The Astrophysical Journal, 891:113 (19pp), 2020 March 10 https://doi.org/10.3847/1538-4357/ab6d76


# Effect of Feedback of Massive Stars in the Fragmentation, Distribution, and Kinematics of the Gas in Two Star-forming Regions in the Carina Nebula

David Rebolledo[1,2], Andrés E. Guzmán[3], Yanett Contreras[4], Guido Garay[5], S.-N. X. Medina[6], Patricio Sanhueza[3], Anne J. Green[7], Camila Castro[8], Viviana Guzmán[9], and Michael G. Burton[10]
[1] Joint ALMA Observatory, Alonso de Córdova 3107, Vitacura, Santiago, Chile; david.rebolledo@alma.cl
[2] National Radio Astronomy Observatory, 520 Edgemont Road, Charlottesville, VA 22903, USA
[3] National Astronomical Observatory of Japan, National Institutes of Natural Sciences, 2-21-1 Osawa, Mitaka, Tokyo 181-8588, Japan
[4] Leiden Observatory, Leiden University, P.O. Box 9513, NL-2300 RA Leiden, The Netherlands
[5] Departamento de Astronomía, Universidad de Chile, Santiago, Chile
[6] Max-Planck-Institut für Radioastronomie, Auf dem Hügel 69, D-53121 Bonn, Germany
[7] Sydney Institute for Astronomy, School of Physics, The University of Sydney, NSW 2006, Australia
[8] Departamento de Ciencias Físicas, Facultad de Ciencias Exactas, Universidad Andres Bello, Av. Fernandez Concha 700, Santiago, Chile
[9] Instituto de Astrofísica, Pontificia Universidad Católica de Chile, Av. Vicuña Mackenna 4860, 7820436 Macul, Santiago, Chile
[10] Armagh Observatory and Planetarium, College Hill, Armagh, BT61 9DG, Northern Ireland, UK
*Received 2019 October 6; revised 2019 December 21; accepted 2020 January 19; published 2020 March 11*

## Abstract

We present ALMA high spatial resolution observations toward two star-forming regions located in one of the most extreme zones of star formation in the Galaxy, the Carina Nebula. One region is located at the center of the nebula and is severally affected by the stellar feedback from high-mass stars, while the other region is located farther south and is less disturbed by the massive-star clusters. We found that the region at the center of the nebula is forming less but more massive cores than the region located in the south, suggesting that the level of stellar feedback effectively influences the fragmentation process in clumps. Lines such as HCN, $HCO^+$, and SiO show abundant and complex gas distributions in both regions, confirming the presence of ionization and shock fronts. Jeans analysis suggests that the observed core masses in the region less affected by the massive stars are consistent with thermal fragmentation, but turbulent Jeans fragmentation might explain the high masses of the cores identified in the region in the center of Carina. Consistently, two different analyses in the $HCO^+$ line provided evidence for a higher level of turbulence in the gas more affected by the stellar feedback. The gas column density probability functions, N-pdf's, show lognormal shapes with clear transitions to power-law regimes. We observed a wider N-pdf in the region at the center of the nebula, which provides further evidence for a higher level of turbulence in the material with a higher level of massive stellar feedback.

*Unified Astronomy Thesaurus concepts:* Star forming regions (1565); Interstellar medium (847); Interstellar molecules (849); Interstellar radiation field (852); Nebulae (1095); Interstellar clouds (834); H II regions (694); Dense interstellar clouds (371)

## 1. Introduction

Star formation occurs almost exclusively in the densest regions of molecular clouds. Supersonic turbulence, stellar feedback, gas self-gravity, and magnetic fields shape the complex density and velocity distributions observed inside molecular clouds (McKee & Ostriker 2007). The relative importance of these mechanisms over a range of physical conditions in the interstellar medium (ISM) is one of the most important open questions in the star formation research community (Federrath et al. 2016). The unprecedented capabilities offered by the Atacama Large Millimeter/submillimeter Array (ALMA) can provide highly resolved and full-flux recovery radio images of star-forming regions in the Milky Way (Rathborne et al. 2015). These images have allowed us to study the connection between the cloud internal structure and the capability of the clouds to form stars, and they provide a better understanding on their wide range of star formation efficiency and rate (Heiderman et al. 2010).

The Carina Nebula Complex (CNC) is a spectacular star-forming region located at a distance of 2.3 kpc (Smith & Brooks 2008), which is close enough to observe faint nebular emission, small-scale structure, and lower-mass protostars. With more than 65 O stars, it is also the nearest analog of more extreme star-forming regions, such as 30 Doradus in the Large Magellanic Cloud. The most stunning features in *Hubble Space Telescope* (Smith et al. 2010b) and *Spitzer* images are the numerous pillar-like mountains of dust, which are situated around the periphery of the H II region and point in toward the central massive-star clusters. Optical and infrared observations have provided ample evidence for active star formation in the dust pillars, with more than 900 young stellar objects identified (Smith et al. 2010a).

Our team has been leading a major effort to map different phases of the ISM across the entire CNC region at different size scales using the Australia Telescope Compact Array (ATCA), the Mopra telescope, and ALMA. We are currently producing high-quality radio images that will provide a unique probe of the relationship between the neutral, ionized, and molecular gas phases of the ISM in the Carina region.

The Mopra CO images, combined with far-infrared data from *Herschel*, have allowed us to determine the overall molecular mass and its distribution across the CNC (Rebolledo et al. 2016). We also reported significant dust temperature variations across the CNC, revealing the strong impact of the massive-star clusters located at the center of the nebula. Detailed comparison between the total gas column density derived from dust emission maps and the molecular column

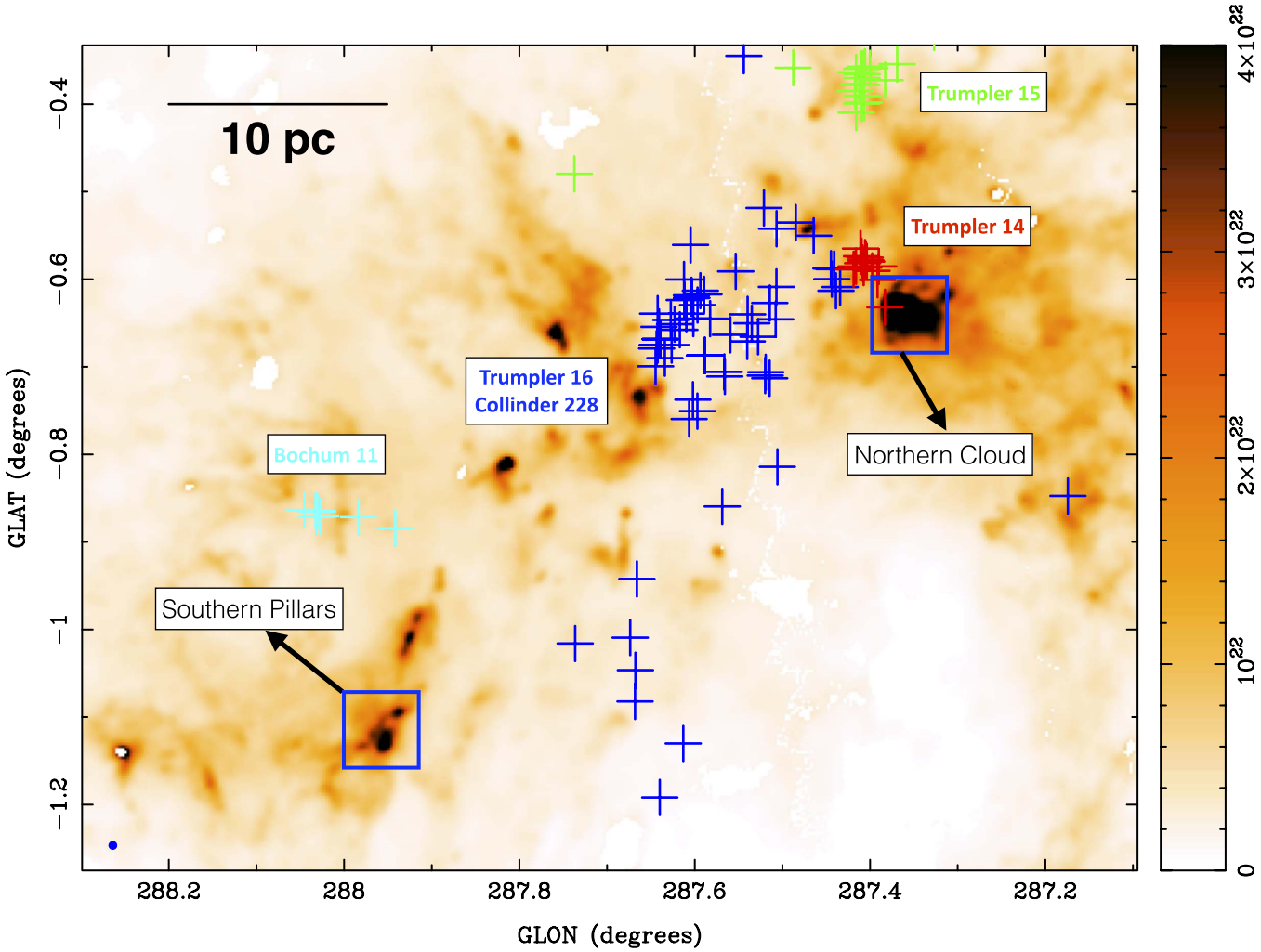


**Figure 1.** Total column density of the CNC derived from *Herschel* infrared maps (Rebolledo et al. 2016). The color bar is in units of $cm^{-2}$. The blue boxes show the location of the regions observed with ALMA, one in the NC and another in the SP. Each box is $\sim 4 \times 4$ $arcmin^2$. The horizontal black line shows the scale of 10 pc. The blue plus signs show the Trumpler 16 and Collinder 228 stellar clusters, red plus signs show Trumpler 14, green plus signs show Trumpler 15, and cyan plus signs show the Bochum 11 cluster, all of them listed in Smith (2006).

density derived from CO maps allowed us to grasp the variation of the $X_{CO}$ factor across the CNC and link this variation to the differences in gas temperature and level of stellar feedback.

In the second paper of the project, we reported high-sensitivity and high-resolution maps of the H I 21 cm line toward the CNC obtained with the ATCA (Rebolledo et al. 2017). This detailed map of the atomic gas revealed a complex filamentary structure across the velocity range that crosses the Galactic disk. Taking advantage of the continuum sources present in the CNC, both diffuse and compact, we were able to identify the cold component of the atomic gas. In some particular cases we determined the line optical depth and the spin temperature, two quantities extremely difficult to obtain from pure line emission maps. Additionally, detection of H I self-absorption revealed the presence of cold neutral gas, signaling the phase transition between atomic and molecular gas and perhaps reservoirs of "dark" molecular gas.

Using the ATLASGAL compact source catalog (Schuller et al. 2009), 60 dense clumps were identified throughout the CNC. Utilizing infrared images, it was found that these clumps span a range of evolutionary stages from protostellar to more evolved H II regions. We performed Mopra observations of a combination of dense gas, shock, and ionization tracers toward all 60 clumps in order to characterize the physical and chemical evolution of high-mass clumps in this region (Contreras et al. 2019). This study showed that the clumps in Carina are warmer, are less massive, and show less emission from the four most commonly detected molecules, $HCO^+$, $N_2H^+$, HCN, and HNC, compared to clumps associated with masers in the Galactic plane (Green et al. 2009; Green et al. 2012; Avison et al. 2016). This result provided support to the scenario in which the high radiation field of nearby massive stars is dramatically affecting its local environment and therefore the chemical composition of the dense clumps.

Among the sample of massive clumps observed in the CNC, one region located in the Southern Pillars (SP) and another located in the Northern Cloud (NC) seem to show very different physical conditions (Roccatagliata et al. 2013; Rebolledo et al. 2016). As can be seen in Figure 1, the region in the NC is in the vicinity of the massive-star clusters Trumpler 14 and Trumpler 16 ($\sim$2.5 pc from the nearest massive stars) and is located in one of the brightest H II regions, Car I (Gardner & Morimoto 1968; Brooks et al. 2001). On the

**Table 1**
Spectral Setup of ALMA Observations

| Line | Transition | Rest Frequency (GHz) | Bandwidth (MHz) | Channel Width (kHz) |
|---|---|---|---|---|
| $H^{13}CN$ | $v = 0$ $J = 1 \rightarrow 0$ | 86.38734 | 58.6 | 61.0 |
| HCO | 1(0,1)–0(0,0) $J = 3/2$–$1/2$ | 86.67076 | 58.6 | 122.1 |
| $H^{13}CO^+$ | $J = 1 \rightarrow 0$ | 86.75428 | 58.6 | 61.0 |
| SiO | $v = 0J = 2 \rightarrow 1$ | 86.84696 | 58.6 | 122.1 |
| HCN | $v = 0J = 1 \rightarrow 0$, $F = 2 \rightarrow 1$ | 88.63184 | 58.6 | 61.0 |
| $HCO^+$ | $v = 0J = 1 \rightarrow 0$ | 89.18852 | 58.6 | 61.0 |
| HNCO | $v = 0$ 4(0, 4)→ 3(0, 3), $F = 5 \rightarrow 4$ | 87.92521 | 58.6 | 122.1 |
| $NH_2CHO$ | 4(1, 3)→ 3(1, 2), $F = 5 \rightarrow 4$ | 87.84887 | 58.6 | 122.1 |
| SO | $3\Sigma v = 0$ 3(2)→ 2(1) | 99.29987 | 58.6 | 122.1 |
| $HCC^{13}CN$ | $J = 11 \rightarrow 10$, $F = 11 \rightarrow 10$ | 99.66146 | 58.6 | 122.1 |
| $NH_2CN$ | $v = 0$ 5(1, 4)→ 4(1, 3) | 100.62950 | 58.6 | 122.1 |
| $CH_3SH$ | $v = 0$ 4(0)→ 3(0) A | 101.13911 | 58.6 | 122.1 |
| Continuum | ⋯ | 99.5 | 2000 | 15,625 |

other hand, the region in the SP is located much farther away (∼30 pc) from the center of the radiation field. The strength of the far-UV radiation in some regions of the NC can be $\sim 7000 G_0$, which is 10 times larger than the radiation field observed in the SP (Brooks et al. 2003; Roccatagliata et al. 2013). The dust temperature map also shows differences between these two regions (Rebolledo et al. 2016). While the dust temperature at the SP varies between ∼20 and 22 K, the NC shows dust temperatures of ∼28–30 K. Thus, these two distinctive regions represent our best choice to investigate the effect of massive-star feedback on the formation of new stars.

In a recent paper, Seo et al. (2019) observed the 158 $\mu$m line of [C II] in the gas nearby Trumpler 14 and the bright H II region Car I using the Stratospheric Terahertz Observatory 2 (STO2). They found that the bright [C II] emission correlates with the surfaces of the CO structures, tracing the photo-dissociation region (PDR) and the ionization fronts in the NC. By comparing [C II] with multiple tracers such as H I 21 cm, CO (1 → 0), and radio recombination lines, they found that the H II region in the NC is expanding freely toward us and that the destruction of the molecular cloud is driven by UV photoevaporation. However, the spatial resolution of 48″ of this study was insufficient to obtain a detailed internal view of the gas in this region.

In this paper, we report ALMA Band 3 observations toward these two distinct regions in the CNC that contain several massive clumps. The science goal was to compare the internal structure of the two selected regions to investigate the effect of massive stellar feedback in the gas kinematics and distribution. The continuum, along with the emission in the $HCO^+$, HCN, SiO, and other lines, is used to determine the location, mass, and kinematics of the small-scale fragments within these regions.

The study is presented as follows: Section 2 describes the observations of the two regions in the CNC with ALMA. Section 3 presents the internal gas distribution and the properties of cores identified in each region. This section also discusses the gas kinematics revealed by each detected line in both regions. Section 4 reports on the differences in the core masses and gives an explanation for this based on Jeans analysis. Finally, this section discusses the level of turbulence in these two regions and its effect on the kinematics properties of the gas and the overall column density distribution in both regions. In Section 5 we provide a summary of the work presented in this paper.

## 2. DATA

### 2.1. ALMA Observations

The observations were conducted during the ALMA Cycle 4 under the project code 2016.1.01609.S. Our goal was to resolve the small-scale structure inside the observed regions in the SP and the NC. We requested a 3″ spatial resolution for our maps, which corresponds to ∼0.03 pc at the distance of 2.3 kpc. Based on the ATLASGAL 870 $\mu$m maps, an area of 4 × 4 arcmin$^2$ (equivalent to 2.7 × 2.7 pc$^2$) is needed to enclose the dust emission in each region. The 12 m and 7 m array observations are requested to maximize flux recovery at scales of ∼1′, similar to the scales observed in the Mopra maps. The mosaic for the 12 m array was composed of 134 pointings, while 46 pointings were needed to cover the same area with the 7 m array. Figure 1 shows the location of the SP and the NC fields covered by our observations. It also shows the position of the massive-star clusters. Four spectral basebands in Band 3 are utilized to observe 12 spectral lines and the continuum. Table 1 details the spectral setup for our observations. For the main lines HCN, $HCO^+$, $H^{13}CN$, and $H^{13}CO^+$, the channel resolution was 61 kHz. For the remaining lines, the channel resolution was 122 kHz. The continuum window was centered in 99.5 GHz, and its bandwidth was chosen to be 2000 MHz in order to maximize sensitivity.

### 2.2. Imaging of 12 and 7 m Data

We downloaded the raw data from the ALMA archive and regenerated the calibrated data for both arrays. Then, the 12 and 7 m array observations were combined and imaged together using the *tclean* task of the CASA package. For the main lines, HCN, $HCO^+$, $H^{13}CN$, and $H^{13}CO^+$, the channel width is 0.41 km s$^{-1}$. For the remaining lines, the velocity resolution is a factor of two larger. The synthesized beam achieved in our maps, with small variations across the different spectral windows, is ∼2.″8 × 1.″8 using a robust weighting of 0.5. The noise in a single channel is 10 mJy beam$^{-1}$. For the continuum maps, the achieved noise is 0.22 mJy beam$^{-1}$ for the NC and 0.12 mJy beam$^{-1}$ for the SP for the 2 GHz window. This correspond to a 3$\sigma$ sensitivity of 1.1 $M_\odot$ for the NC and 0.8 $M_\odot$ for the SP.

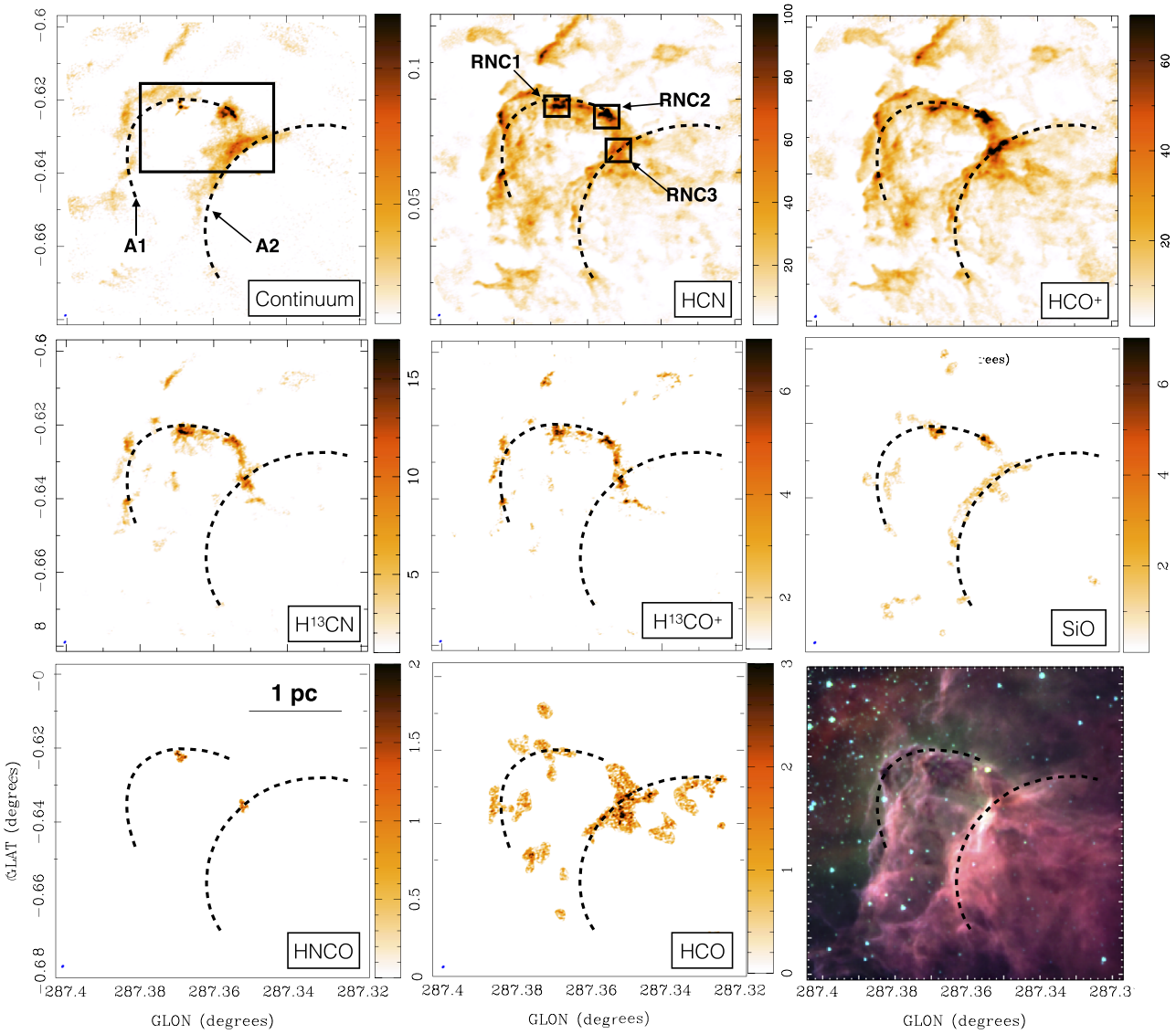


**Figure 2.** Integrated intensity maps of the different tracers observed in NC. The color bar in the continuum image is in K, while the color bars in the line-integrated intensity maps are in units of K km s$^{-1}$. The black dashed lines show the two arc-like features identified in the continuum map, A1 and A2. Those lines have been drawn in the integrated intensity line maps to help comparison. The black rectangle in the map (top left) illustrates the area shown in Figure 3. The small black squares in the HCN map (top middle) show the areas used to generate the spectra shown in Figure 6. The horizontal black line in the HNCO map (bottom left) shows the 1 pc scale at the CNC distance. The bottom-right panel shows a red, green, and blue (RGB) composite image toward the NC. Red is 8.0 $\mu$m, green is 4.5 $\mu$m, and blue is 3.6 $\mu$m from *Spitzer*.

## 3. Results

### 3.1. Morphology of the Emission in the NC and SP

#### 3.1.1. Continuum

Figure 2 shows the continuum map of the region observed in the NC. Two arc-like structures are identified across the surveyed area in the NC, which we named A1 and A2. We suspect that the radiation field from the nearby massive stars is producing ionization fronts that heat the dust in these regions, and our ALMA continuum observations are tracing the front edge of the heated gas. However, a free–free component could also be contributing to the continuum emission.

In the NC region, three bright cores have been identified by visual inspection. Two of the cores are located in close proximity (see Figure 3 for a more detailed image). Table 2 provides the properties of the cores detected in this region. In order to get the integrated flux and size for each core, a 2D Gaussian and a flux offset level have been fitted to each core using the task *imfit* from the Multichannel Image Reconstruction (MIRIAD) package. The strongest emission core, NC1, is located at ($l$, $b$) $\sim$ (287.°369, $-$0.°622) and has an integrated flux of 14.4 mJy. The companion core, NC2, has an integrated flux of 8.07 mJy and is located at 5.″2 away from NC1, which corresponds to $5.8 \times 10^{-2}$ pc at the assumed Carina Nebula distance. The third core, NC3, is located at ($l$, $b$) $\sim$ (287.°355, $-$0.°624), which is 0.6 pc away from NC1 and NC2. NC3 has an integrated flux of 9.78 mJy, and it is surrounded by diffuse emission.

The continuum map toward SP is shown in Figure 4. In this case, no continuum diffuse emission is detected in the SP, which is in contrast with the situation observed in the NC. In total, 10 compact sources are distinguished, a factor of $\sim$3 more than in the NC. Two distinct regions are located at the top and the bottom of the surveyed area, having five cores each.

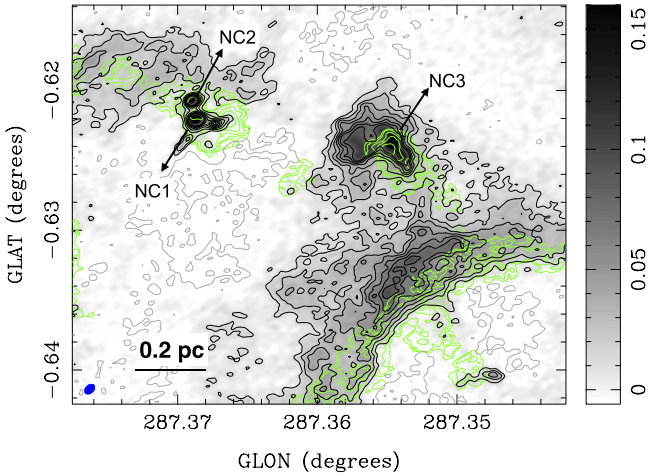


**Figure 3.** Zoomed-in view of the region shown in Figure 2. The black-and-white map is the continuum, with color bar in K. The blue ellipse in the lower left corner shows the ALMA synthesized beam. Gray (negative) and black (positive) contours show $-6\sigma$, $-3\sigma$, $3\sigma$, $6\sigma$, $9\sigma$, $12\sigma$, $15\sigma$, $18\sigma$, and $21\sigma$ levels in the continuum map, with $\sigma$ equal to 4 mK. Green contours show the SiO integrated intensity levels 0.5, 1, 2, 4, 8 and 16 in units of K km s$^{-1}$. Three cores are detected in the continuum emission map. SiO is detected nearby the compact sources, probably associated with outflows. The diffuse SiO follows the arc-like structure A2 traced by the continuum emission, but it is spatially shifted. The continuum emission seen in A2 might be dominated by the ionized gas rather than hot dust emission. Thus, while the continuum emission traces the ionization front produced by the nearby massive stars, the SiO traces the PDR/shock front region.

**Table 2**
Flux Properties of the Cores Identified in the NC and the SP

| Name | Flux (mJy) | FWHM $\theta_{maj}$ (arcsec) | FWHM $\theta_{min}$ (arcsec) |
|---|---|---|---|
| | NC | | |
| NC1 | 14.40 ± 0.92 | 2.33 | 1.23 |
| NC2 | 8.07 ± 0.80 | 1.68 | 0.85 |
| NC3 | 9.78 ± 3.3 | 2.80 | 0.69 |
| | SP | | |
| SP1 | 2.60 ± 0.40 | 2.70 | 1.12 |
| SP2 | 2.16 ± 1.01 | 4.04 | 0.74 |
| SP3 | 4.29 ± 1.43 | 5.03 | 3.69 |
| SP4 | 1.21 ± 0.45 | 1.95 | 1.29 |
| SP5 | 1.17 ± 0.41 | 2.11 | 0.72 |
| SP6 | 1.15 ± 0.34 | *3.95* | *1.61* |
| SP7 | 1.15 ± 0.34 | 1.28 | 0.54 |
| SP8 | 1.25 ± 0.46 | *2.74* | *2.36* |
| SP9 | 1.23 ± 0.63 | *2.79* | *2.42* |
| SP10 | 1.57 ± 0.49 | *3.25* | *2.05* |

**Note.** The size of cores has been deconvolved with the synthesized beam. Italic font shows unresolved cores.

Figure 5 shows zoomed-in images toward the two groups. Table 2 provides the properties of the cores detected toward SP.

In the region located in the northern part of the SP, a single core, SP1, and two double systems formed by SP2-SP3 and SP4-SP5 pairs are detected (see Figure 5). SP1, SP2, and SP3 have fluxes of 2.60, 2.16, and 4.29 mJy, respectively, and represent the brightest cores in the SP sample. SP4 and SP5 have fluxes of ∼1.2 mJy. The projected distances between the SP1 and the SP2-SP3 and SP4-SP5 pairs are 0.2 and 0.5 pc, respectively. The distance between SP2 and SP3 is $6 \times 10^{-2}$ pc, while the projected distance between SP4 and SP5 is $3 \times 10^{-2}$ pc. In this region we do not detect SiO emission associated with the cores or diffuse emission related to PDRs as observed in the NC.

The group located in the southern part of the SP also has five compact sources identified in the continuum map. There is a triple system formed by SP6, SP7, and SP8. SP6 and SP7 are barely distinguishable from each other, while SP8 is located at $\sim 7.3 \times 10^{-2}$ pc away. Different from the area in the north of the SP, in this region SiO emission is detected (Figure 3). The fluxes of the cores are ∼1.2 mJy.

Located at 0.36 pc away and toward the south from the triple system described above, we identify another core, SP10. Located at 0.14 pc away from it, another core is identified, SP9, and it seems to be connected to SP10. Both cores have fluxes of ∼1.2 mJy.

Although a less massive core could be identified by structure decomposition algorithms such as dendrograms or clumpfind, for the NC we have decided to keep only the three compact sources with obvious round shape and high signal-to-noise ratio (>10). Thus, the cores are sufficiently bright to be differentiated from the diffuse continuum emission. Because the diffuse continuum emission detected in the NC can have a significant component from ionized gas rather than hot dust, structures with lower signal-to-noise ratio might be misidentified as low-mass cores.

### 3.1.2. Molecular Lines

Figures 2 and 4 also show the integrated intensity maps of the observed molecular lines in the NC and SP, respectively. In the following paragraphs, we will discuss in more detail the maps of each detected line individually.

*HCN*.—This line is the brightest in our sample, achieving an integrated intensity peak of ∼218 K km s$^{-1}$ in the NC and 22 K km s$^{-1}$ in the SP, a factor of ∼10 weaker. In general, the peaks of the line are spatially coincident with the position of the cores detected in the continuum. A complex distribution of the emission is seen in the HCN map in both regions, revealing structures that seem to point into the direction of the massive stars. In both regions it is possible to detect profuse low brightness emission. This emission is probably associated with low/moderate column density gas. HCN has already been linked to moderate gas density in molecular clouds (Stephens et al. 2016; Kauffmann et al. 2017). In Goldsmith & Kauffmann (2017), the authors proposed that electron excitation could be responsible for the large spatial extent of emission from dense gas tracers in some molecular clouds, especially in external regions being exposed to high radiation fields. This might be the case of the NC and SP regions. Additionally, we identify a region where no continuum emission is detected but HCN is strong in the SP (red square in Figure 4). We suspect that in this region some cores might be present, but the current sensitivity of our observations is not capable of detecting them.

*$HCO^+$*.—The spatial distribution of $HCO^+$ is remarkably similar to the emission distribution of HCN in both regions. $HCO^+$ shows an integrated intensity peak of ∼120 K km s$^{-1}$ in the NC and 34 K km s$^{-1}$ in the SP, which is a factor of 6 weaker. The two arc-like structures A1 and A2 are evident in the $HCO^+$ map of the NC region, but in this case the diffuse emission inside the cavities makes the identification slightly difficult. As HCN, $HCO^+$ traces not only material associated with the densest gas but also lower-density diffuse gas. As with

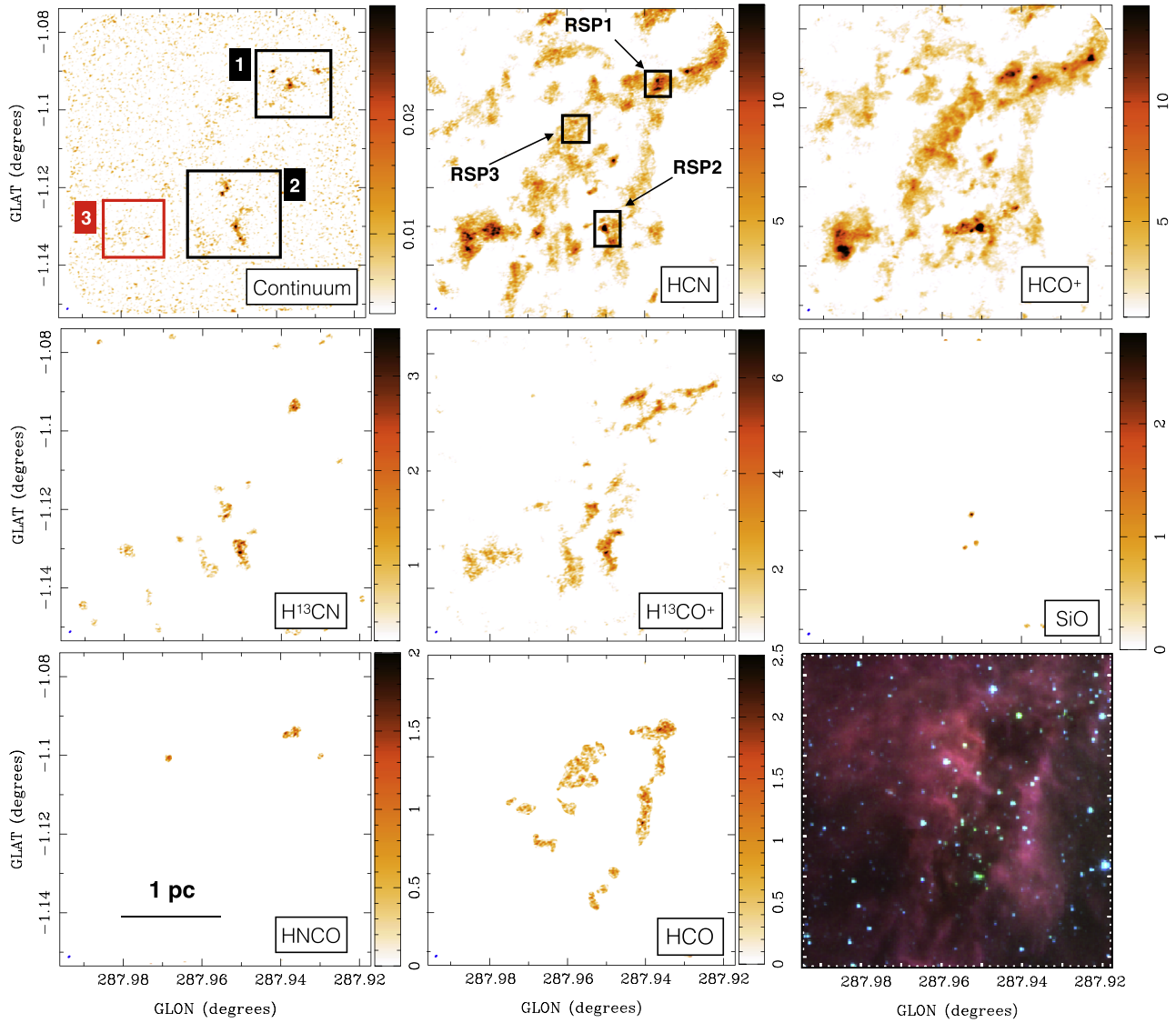


**Figure 4.** Integrated intensity maps of the different tracers observed in SP. The color bar in the continuum image is in K, while the color bars in the line-integrated intensity maps are in units of K km s$^{-1}$. The black rectangles (labeled 1 and 2) in the continuum map (top left) illustrate the zoomed-in areas shown in Figure 5. The red rectangle (labeled 3) shows a region where the continuum is not detected but the lines HCN and HCO$^+$ are bright. The small black squares in the HCN map (top middle) show the areas used to generate the spectra shown in Figure 8. The horizontal black line in the HNCO map (bottom left) shows the 1 pc scale at the CNC distance. The bottom-right panel shows an RGB composite image toward the NC. Red is 8.0 $\mu$m, green is 4.5 $\mu$m, and blue is 3.6 $\mu$m from *Spitzer*.

the HCN molecule, Goldsmith & Kauffmann (2017) find that the HCO$^+$ molecule is also similarly affected by electron excitation. This is consistent with both lines showing similar emission distributions.

*$H^{13}CN$ and $H^{13}CO^+$.*—The H$^{13}$CN and H$^{13}$CO$^+$ lines show almost identical features in the NC. The distributions of H$^{13}$CN and H$^{13}$CO$^+$ are less diffuse than those of HCN and HCO$^+$, as they trace denser gas. The only arc-like structure traced by both H$^{13}$CN and H$^{13}$CO$^+$ is A1. The A2 arc is not visible in any of the integrated intensity maps of H$^{13}$CN or H$^{13}$CO$^+$. We propose that this difference is related to abundance differences of the H$^{13}$CN and H$^{13}$CO$^+$ isotopologues between the two arcs. If it is assumed that the gas in A2 is less dense, then the less abundant isotopologues suffer from stronger reduction in abundance due to selective photodissociation (Keene et al. 1998).

On the other hand, in the SP the morphologies of H$^{13}$CN and H$^{13}$CO$^+$ are different. While H$^{13}$CO$^+$ shows extended emission that approximately follows the filamentary structure of the diffuse gas traced by HCO$^+$, H$^{13}$CN is only detected toward the cores identified in the continuum. This is likely a sensitivity effect, as the H$^{13}$CN is weaker (likely because the intensity is shared among the hyperfine lines) and we only see the peaks where the column density is probably higher. The difference in brightness does point to a difference in radiation field or chemistry. The fact that the difference is not as pronounced in the main isotopologues (HCN and HCO$^+$) is probably due to line opacity.

*SiO.*—In the case of SiO, compact emission associated with the cores and diffuse emission that follows A2 arc-like structure are detected in the NC. Figure 3 shows a zoomed-in image toward the position of the three cores detected in the continuum map overlaid with the SiO map. SiO is seen around the three cores, probably associated with outflows of protostars inside the cores. The arc-like structures traced by the diffuse SiO are intrinsically related to the PDR of the shock front

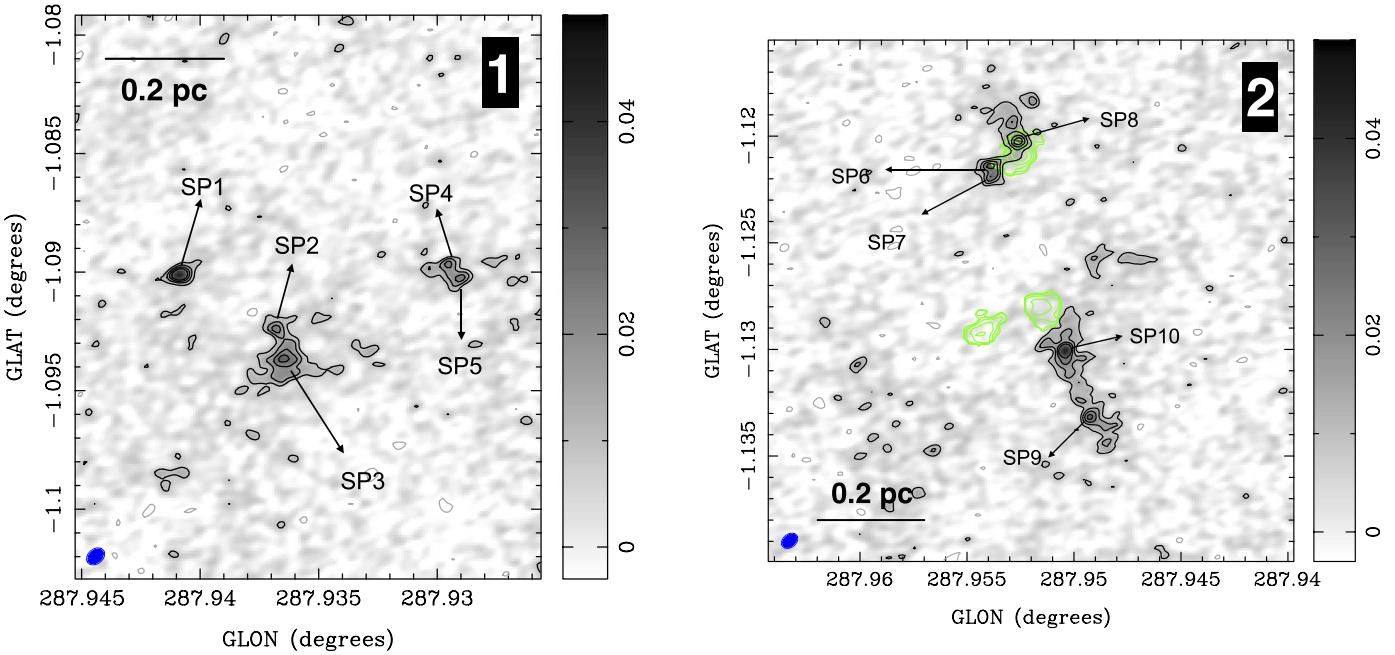


**Figure 5.** Zoomed-in view of the squares 1 and 2 shown in the continuum map in Figure 4. The black-and-white map is the continuum, with color bar in K. The blue ellipse in the lower left corner shows the ALMA synthesized beam. Gray (negative) and black (positive) contours show $-3\sigma$, $3\sigma$, $5\sigma$, $7\sigma$, and $9\sigma$ levels in the continuum map, with $\sigma$ equal to 3 mK. Green contours show the SiO integrated intensity levels 0.12, 0.24, 0.48, 0.96, and 1.92 in units of K km s$^{-1}$. Ten cores are detected in the continuum emission map. SiO is detected nearby some compact sources, probably associated with outflows. Different from the NC, continuum and SiO diffuse emission are not detected.

produced by the energy feedback of the nearby massive stars. Detection of diffuse SiO has been reported in several previous studies related to stellar feedback. For example, Schilke (2001) reported observations of the SiO toward several PDRs, including the Orion bar and S140. They found that the distribution of the SiO emission is somewhat more extended than arising from just the layer of the gas associated with the ionization front. More remarkably, a significant shift between the position of the continuum and the SiO emission is seen in A2 (Figure 3). A possibility is that the continuum emission seen in A2 is dominated by ionized gas rather than hot dust emission. Thus, A2 traces the ionization front produced by the nearby massive stars, while the SiO traces the PDR/shock front region.

In contrast to the NC, in the SP diffuse SiO is not seen. We only detect three weak and compact sources, probably linked to cores SP7, SP8, and SP10 (see Figure 5). This establishes a clear difference between the NC and the SP in terms of the effect of external stellar feedback between the two regions: NC is being heavily affected by the radiation field of the nearby massive stars, producing ionization flux that removes the Si from the dust grains and puts it into gas phase. On the other hand, because the SP is less affected by the massive stars relative to NC, no PDRs are present in the ISM, resulting in less Si in gas phase, reducing the emission of diffuse SiO.

*HCO*.—HCO is detected in some of the PDRs reported above in the other lines, with a peak of integrated intensity of $\sim$4 K km s$^{-1}$ in the NC and $\sim$2.2 K km s$^{-1}$ in the SP. In the NC, the line is not detected over the full extent of the fronts, but it is seen in the central part of the field, where the $HCO^+$ line emission is strong in A2 (see Section 3.2.1 for the detected spectra). In the SP, HCO emission is clearly seen in the region where SP2 and SP3 cores are located. Additionally, HCO emission is detected in regions that seem to be located at the surface layers of the SP, especially in the right edge of the cloud. The emission in the center of the field seems to correspond to gas in the foreground of the main cloud and thus exposed to the radiation field coming from the north (see Section 3.2.1 for more details). The formyl radical has been linked to the basic ISM chemistry because its formation is related to abundant molecules such as $HCO^+$ and $CH_2$. The detection of HCO has been previously reported in PDRs regions (Schenewerk et al. 1988; Schilke 2001; Gerin et al. 2009), which is consistent with the detections reported here.

*HNCO*.—HNCO is only detected in regions associated with cores NC1 and NC2 and at the center of A2. No diffuse emission is detected in the NC. HNCO can trace shocks, but it is also detected in PDRs and dense gas in general (Zinchenko et al. 2000; Rodríguez-Fernández et al. 2010; Sanhueza et al. 2012). In the case of the NC, we only detect some compact emission near the continuum cores. This is consistent with the picture where HNCO is a good tracer of hot cores. Thus, our observations suggest that hot core activity is present in our reported cores within the NC. No strong detections of the HNCO line are obtained in the SP.

### 3.2. Gas Kinematics

To study the kinematics of the region observed in the NC and the SP, we obtained the average spectra in selected regions associated with different structures. The size of each box used to extract the spectra is 20″. Only the lines with detections are included, namely, HCN, $HCO^+$, $H^{13}CN$, $H^{13}CO^+$, SiO, HCO, and HNCO.

#### 3.2.1. Northern Cloud

The regions selected in the NC are labeled as RNC1, RNC2, and RNC3, and their locations are indicated in Figure 2. The

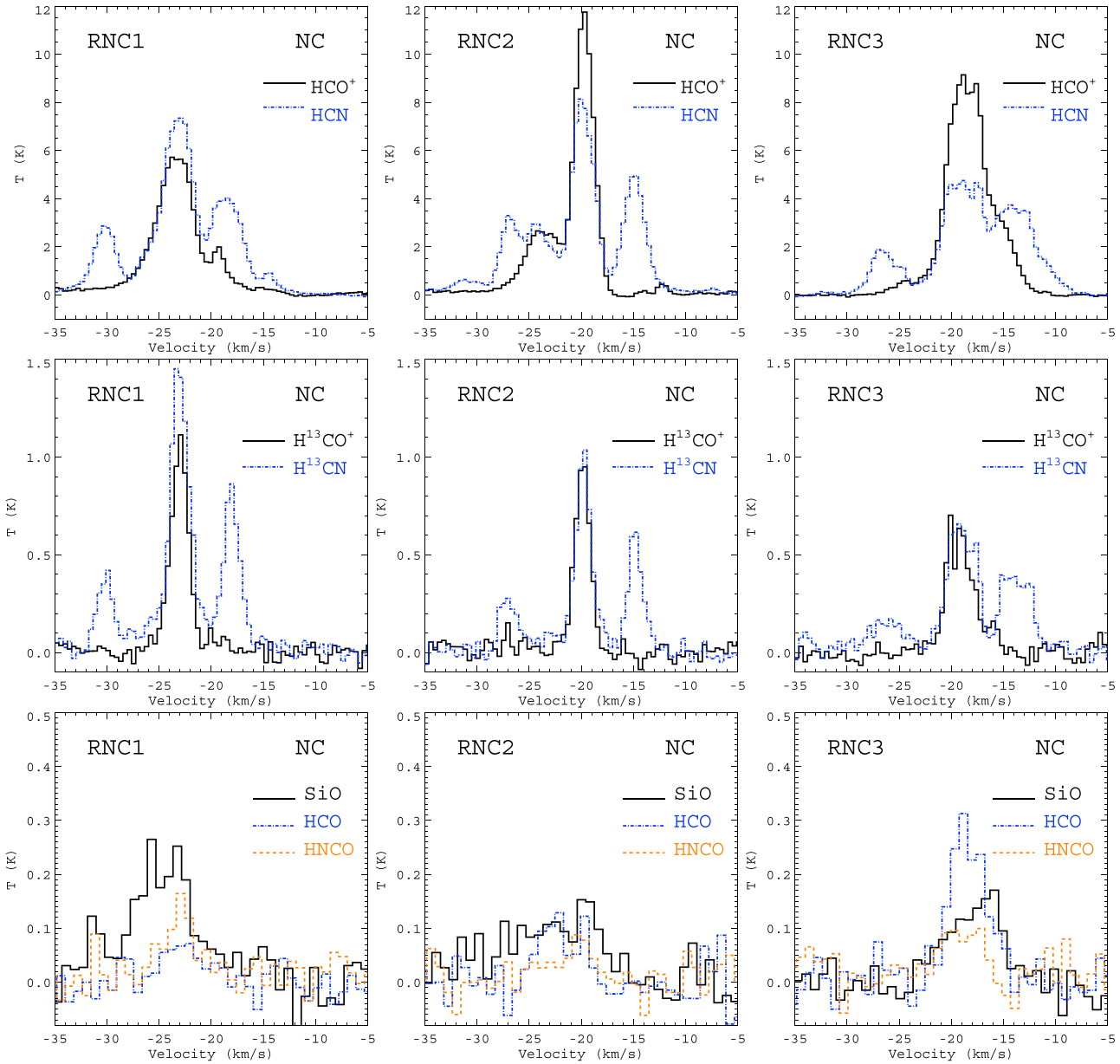


**Figure 6.** Average spectra of the detected lines toward three representative regions in the NC. The regions RNC1, RNC2, and RNC3 are shown in Figure 2. HCN and $HCO^+$ are the brightest lines among the sample, and they show a complex velocity field in the NC. Hyperfine structures of HCN and $H^{13}CN$ are clearly detected.

spectra are shown in Figure 6. Figure 7 shows a velocity decomposition of the emission for $HCO^+$, $H^{13}CO^+$, and SiO lines. Four velocity ranges were selected in order to show a better picture of the different components present in the gas.

In RNC1, which is located where the cores NC1 and NC2 are identified, a main component at $\sim -23\,km\,s^{-1}$ in all the molecular lines is detected. This bright and broad component corresponds to the excited gas front pointing to the Trumpler 14 cluster as shown in Figure 7. A second lower-intensity component at $\sim -19\,km\,s^{-1}$ is also identified in the $HCO^+$ and HCN spectra. This component is part of another PDR front that appears at $\sim -19\,km\,s^{-1}$ and that is more evident in RNC2 (see below). In the velocity range from $-35.0$ to $-21.3\,km\,s^{-1}$, the ionization front coming from Trumpler 14 has shaped the $HCO^+$ as a large arc-like structure. The SiO is detected along the photoionization region in the arc-shaped gas and in many other small compact sources, signalizing the position of ionization regions and/or outflows.

RNC2 is located near the center of the covered field, and two components in the HCN and $HCO^+$ spectra are seen. The strongest component shows a peak at $\sim -19.5\,km\,s^{-1}$ and corresponds to another photoionization region seen in the velocity range from $-21.3$ to $-18.4\,km\,s^{-1}$. The second component is the continuation of the emission observed in RNC1.

In RNC3 the predominant component as seen in $HCO^+$ and HCN is still located at $\sim -19.5\,km\,s^{-1}$, but another weaker component at $-17\,km\,s^{-1}$ is seen. This weaker component is related to another PDR front that is seen in the velocity range from $-18.4$ to $-13.1\,km\,s^{-1}$ (Figure 7). The front is not detected in $H^{13}CO^+$ and $H^{13}CN$, suggesting that the gas in this region is less dense. SiO is detected in the spectrum of RNC3, and Figure 7 shows that this line nicely traces the full extent of

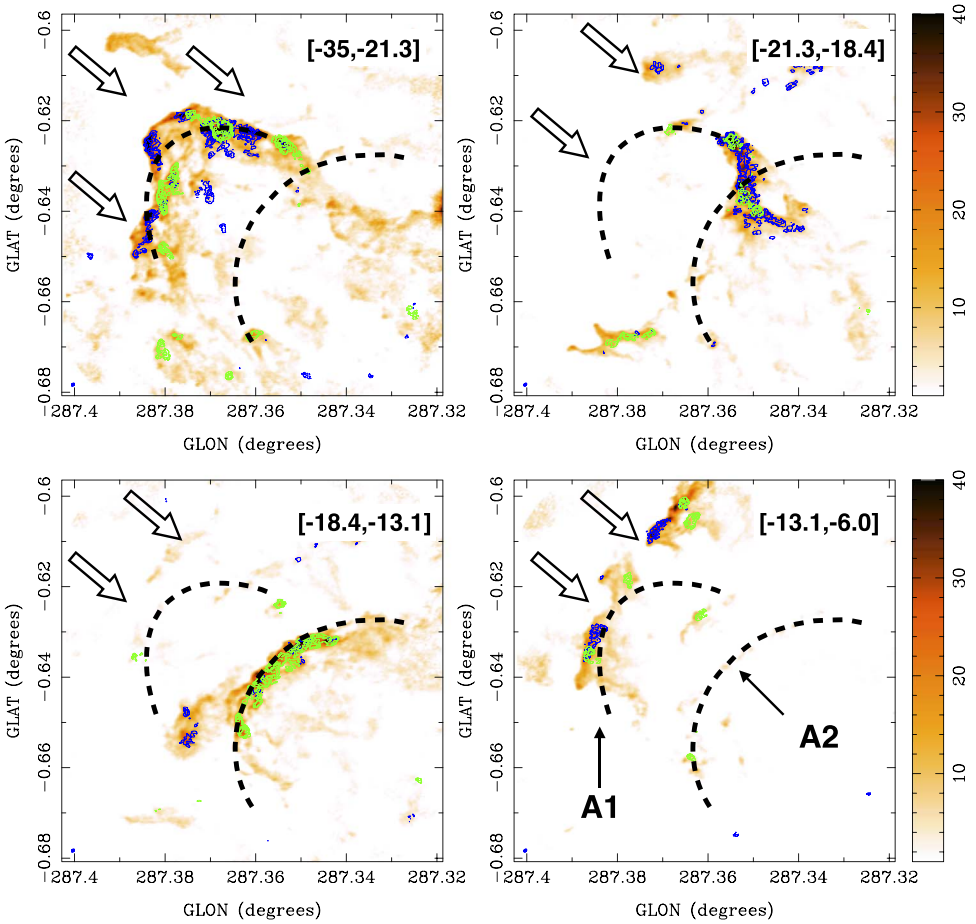


**Figure 7.** Velocity decomposition of the line emission in the NC. Each panel shows integrated intensity maps over the velocity range shown in the upper right corner in km s$^{-1}$. The velocity ranges are selected in order to show different gas shock fronts. The color images are the integrated intensity of the $HCO^+$ in K km s$^{-1}$. The blue contours show the $H^{13}CO^+$ levels at 1, 2, 4, 8, 16, 32, and 64 K km s$^{-1}$. The green contours show SiO integrated intensity levels at 0.5, 1, 2, 4, 8, 16, 32, and 64 K km s$^{-1}$. The white arrows show the approximate direction of the radiation front coming from the Trumpler 16 and Trumpler 14 clusters shown in Figure 1.

the front. The front has an arc-like shape pointing to the direction of the radiation from Trumpler 14 and follows one of the structures identified in the continuum emission map as discussed in Section 3.1.2. HCO is much brighter in RNC3 than in RNC1 and RNC2. It is possible that RNC3 is more illuminated by radiation than the other two regions.

Figure 7 also reveals an additional gas front in the velocity range from −13.0 to −6.0 km s$^{-1}$. This front is almost perpendicular to the projected direction of the radiation field from Trumpler 14 and is detected in $HCO^+$ and HCN. The strongest emission in these lines is detected between −12.5 and −9 km s$^{-1}$. SiO is also detected in some of the regions along the front.

### 3.2.2. Southern Pillars

Figure 8 shows the spectra of the detected lines toward the three selected regions in the SP: RSP1, RSP2, and RSP3. These three regions, shown in Figure 4, include the regions with bright emission in the lines HCN and $HCO^+$. Additionally, Figure 9 shows a velocity decomposition of the line emission for $HCO^+$, $H^{13}CO^+$, and SiO. Two velocity ranges are selected, from −25 to −19 km s$^{-1}$ and from −19 to −13 km s$^{-1}$, in order to better show the emission associated with the two components present in the region.

The RSP1 region encompasses cores SP2 and SP3. A single component at ∼−22.5 km s$^{-1}$ is seen in the $HCO^+$ and HCN spectra, which also show the hyperfine lines. We detect strong emission in the $H^{13}CO^+$ spectrum, but the $H^{13}CN$ counterpart is very weak. Both HCO and HNCO are detected in this region. We notice that RSP1 is the only region in SP that shows HNCO emission. Figure 9 shows that the majority of the flux in the SP is in the velocity range from −25 to −19 km s$^{-1}$, and we define this as the main cloud.

RSP2 covers the region associated with SP9 and SP10. Both $HCO^+$ and HCN show a strong self-absorption feature in the profiles at ∼−22.5 km s$^{-1}$. This might correspond to cold and dense gas located in the region where the cores SP9 and SP10 are identified. On the other hand, $H^{13}CO^+$ and $H^{13}CN$ show emission profiles at the same velocity of ∼−22.5 km s$^{-1}$ as the self-absorption features detected in $HCO^+$ and HCN. A likely explanation of this could be a signature of gas expansion in the cores. Marginal detection for the HCO line is observed. This velocity component belongs to the main cloud already observed in RSP1.

Finally, we have chosen RSP3 as the region that shows the second velocity component at −18 km s$^{-1}$. This component is seen in the $HCO^+$ spectrum. In the case of HCN, the main line is almost totally suppressed while the satellite lines are detected. Observations of anomalies in the HCN hyperfine line strengths have been reported in previous works (Guilloteau & Baudry 1981; Loughnane et al. 2012; Mullins et al. 2016). Several mechanisms have been proposed to explain the

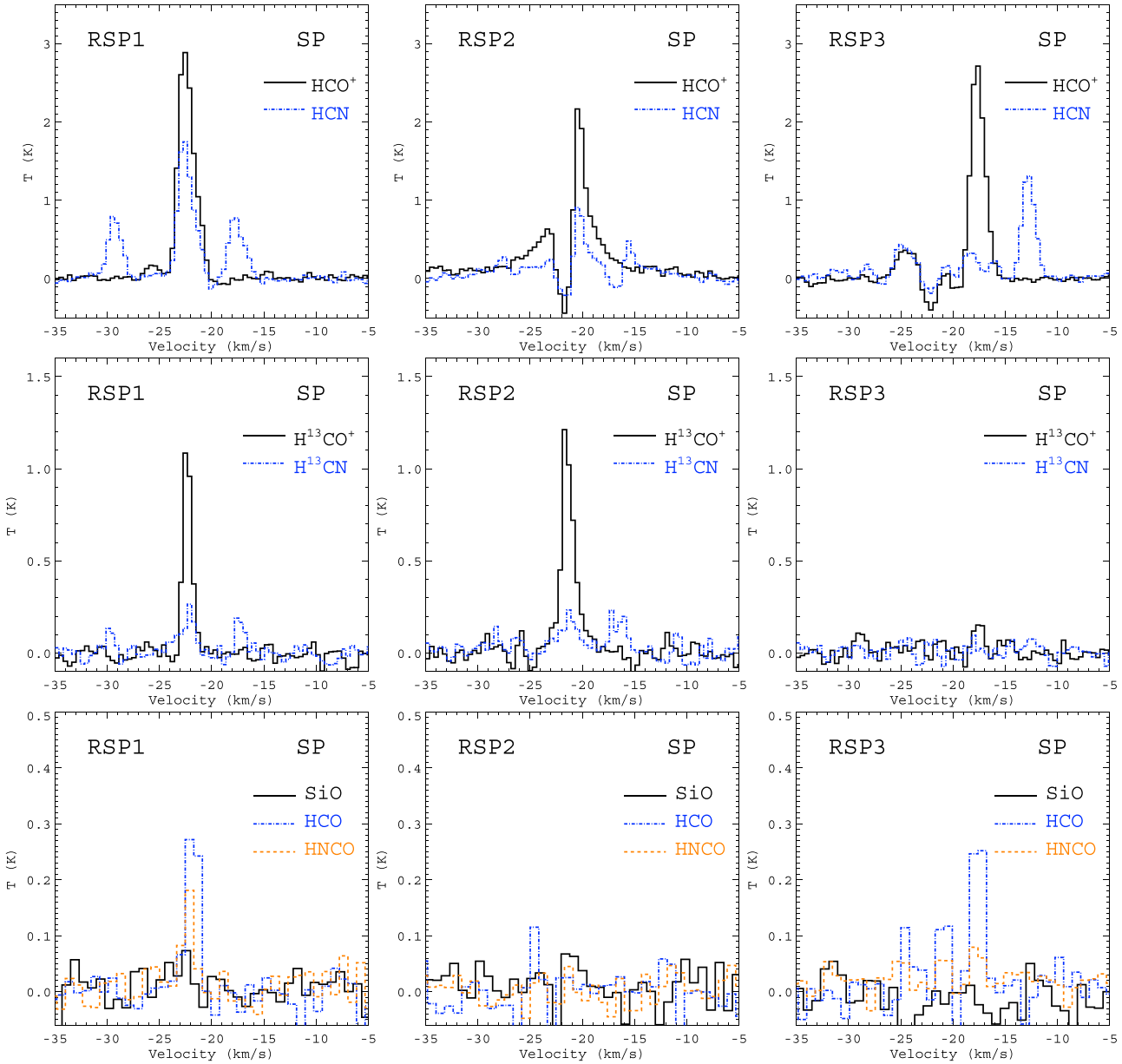


**Figure 8.** Average spectra of the detected lines toward three representative regions in the SP. The regions RSP1, RSP2, and RSP3 are shown in Figure 4. As in NC, the brightest lines are the HCN and $HCO^+$. In addition, HCN hyperfine structures are detected in all the regions. RSP2 and RSP3 present self-absorption features at $-22$ km s$^{-1}$ in both HCN and $HCO^+$. In RSP3, we observe a total suppression of the main line of HCN, but the hyperfine lines are still detected. On the other hand, $H^{13}CN$ and $H^{13}CO^+$ are not detected in RSP3, but weak emission of HCO is observed.

deviation of the hyperfine line ratios from local thermodynamic equilibrium (LTE) conditions. In their study of low- and high-mass star-forming cores, Loughnane et al. (2012) found that HCN hyperfine anomalies are common in both types of cores. They proposed that these anomalies are produced by the line-overlap effect. By modeling the HCN hyperfine line emission, Mullins et al. (2016) found, on the other hand, that HCN line ratios are highly dependent on the optical depth. We suspect that in the case of region RSP3 in SP, the high opacity of the HCN line and low temperature might be responsible for the reduction of the main line, but why a similar effect is not observed in the hyperfine lines is still unknown. $H^{13}CO^+$, $H^{13}CN$, SiO, and HNCO are not detected in this region. On the other hand, HCO emission is detected.

## 4. Discussion

### 4.1. Masses of the Cores

Table 3 gives the masses and sizes of each core identified in SP and NC. The former were computed assuming dust temperature values of 23 K for the SP and 28 K for the NC, both reported in Rebolledo et al. (2016). We used a dust opacity $\kappa_{3\,\mathrm{mm}} = 0.186\,\mathrm{cm^2\ g^{-1}}$ computed from extrapolation of $\kappa_{1.3\,\mathrm{mm}} = 1\,\mathrm{cm^2\ g^{-1}}$ and assuming $\beta = 2$. A gas-to-dust ratio of 100 was assumed. The sizes were calculated following Solomon et al. (1987) and Rosolowsky & Leroy (2006). The core radius, $R_c$, is calculated by using $R_c = 1.91\sigma_r$, where $\sigma_r$ is the *rms* size of the clump.

As was described in Section 3, we identified three cores in the NC (NC1–NC3) and 10 in the SP (SP1–SP10). In terms of the masses, the NC has the most massive cores compared to the

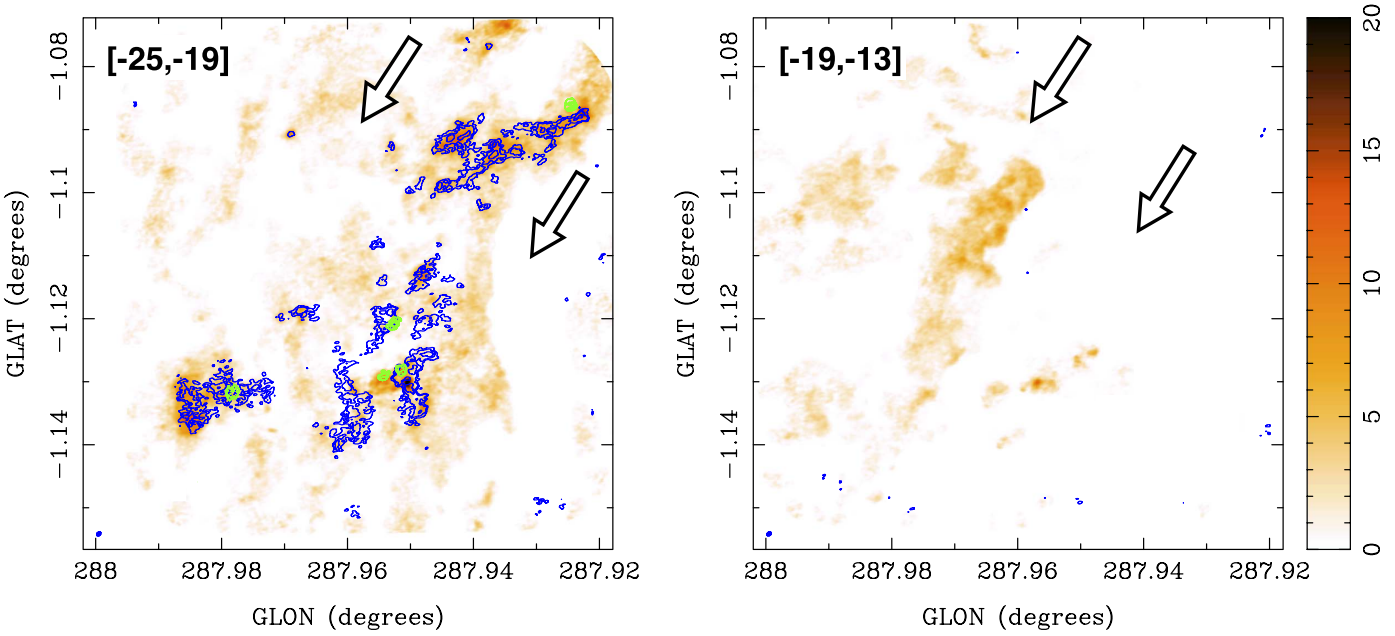


**Figure 9.** Velocity decomposition of the line emission in the SP. Each panel shows integrated intensity maps over the velocity range shown in the upper left corner in km s$^{-1}$. The velocity ranges are selected in order to show different gas shock fronts. The color images are the integrated intensity of the $HCO^+$ in K. The blue contours show the $H^{13}CO^+$ levels at 1, 2, 4, and 8 K km s$^{-1}$. The green contours show SiO integrated intensity levels at 0.12, 0.24, 0.48, 0.96, and 1.92 K km s$^{-1}$. The white arrows show the approximate direction of the radiation front coming from nearby massive-star clusters shown in Figure 1.

**Table 3**
Physical Properties of the Cores Identified in the NC and the SP

| Name | Mass ($M_\odot$) | Radius $R_c$ (pc) |
|---|---|---|
| | NC | |
| NC1 | 25.0 | 0.015 |
| NC2 | 14.0 | 0.011 |
| NC3 | 17.0 | 0.013 |
| Mean | 19.4 | 0.013 |
| Total | 58.3 | ... |
| | SP | |
| SP1 | 5.6 | 0.016 |
| SP2 | 4.7 | 0.016 |
| SP3 | 9.3 | 0.039 |
| SP4 | 2.6 | 0.014 |
| SP5 | 2.5 | 0.011 |
| SP6 | 2.5 | *0.023* |
| SP7 | 2.5 | 0.008 |
| SP8 | 2.7 | *0.023* |
| SP9 | 2.6 | *0.023* |
| SP10 | 3.4 | *0.023* |
| Mean | 3.8 | *0.020* |
| Total | 38.4 | ... |

**Note.** Italic font shows unresolved cores.

SP. While the NC has a mean core mass of 19.4 $M_\odot$, the mean in the SP is 3.8 $M_\odot$, a factor of 5 difference. The total mass in cores in the NC is 58.3 $M_\odot$, while in the SP it is 38.4 $M_\odot$.

### 4.2. Fraction of the Mass in Cores

In this section we estimate the percentage of the total mass inside the cores for both regions. The fraction of mass in cores is an important parameter for the estimation of the star formation efficiency, which is defined as star formation rate per unit of mass. Our motivation is to look for differences in the core mass fraction between the SP and the NC. We start by estimating the total mass within the regions observed in the SP and the NC using the gas column density map derived in Rebolledo et al. (2016) from *Herschel* maps. Because the total mass includes both dense and diffuse gas, we also estimate the gas mass above a certain gas column density threshold, $N_{\rm gas,th}$. As $N_{\rm gas,th}$ is increased, the estimated mass will be composed of denser gas. Finally, the fraction of mass in cores is calculated by dividing the total mass in cores (estimated in Section 4.1) by the gas mass above the different $N_{\rm gas,th}$ values,

$$f_{\rm core\text{-}mass} = \frac{M_{\rm cores}}{M(N_{\rm gas} > N_{\rm gas,th})}, \quad (1)$$

where $M_{\rm cores}$ is the mass in cores and $M(N_{\rm gas} > N_{\rm gas,th})$ is the total mass considering the material above $N_{\rm gas,th}$. Figure 10 shows the relation between $f_{\rm core\text{-}mass}$ and $N_{\rm gas,th}$. The fraction of the mass in cores is slightly higher in the SP than the NC for the same value of $N_{\rm gas,th}$. In both regions, SP and NC, $f_{\rm core\text{-}mass}$ is close to 1% when all the gas mass in the region is considered. As the gas column density threshold to estimate the mass in denser gas increases, the core mass fraction naturally increases. For the SP, $f_{\rm core\text{-}mass}$ reaches a value of ~10% for $N_{\rm gas} = 4 \times 10^{22}$ cm$^{-2}$. At the same column density threshold, the core mass fraction in the NC is still ~1%. Only when we calculate the gas mass above $N_{\rm gas} = 10^{23}$ cm$^{-2}$ does the core mass fraction in the NC reach a value of 16%. Thus, the $N_{\rm gas,th}$ at which a similar $f_{\rm core\text{-}mass}$ value is achieved is a factor of 2.5 larger in the NC than in the SP, showing another clear difference between these two regions.

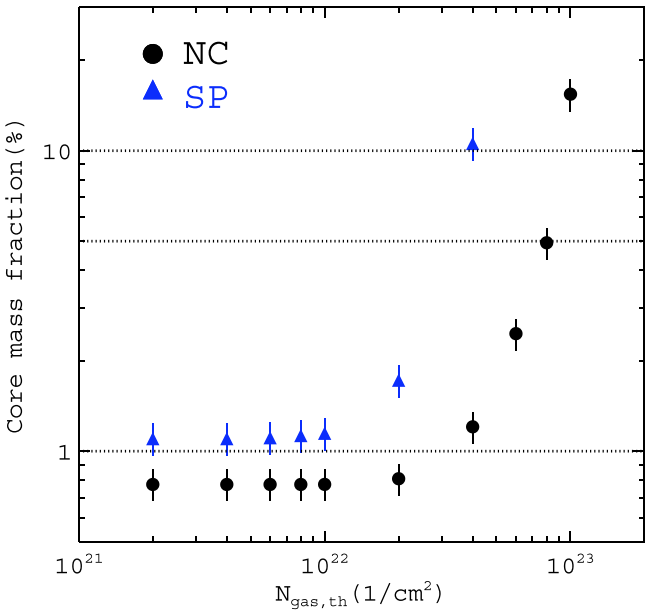


**Figure 10.** Fraction of the mass in cores with respect to the total mass calculated above a given column density threshold. Black circles shows the core mass fraction in the NC, while the blue triangles show the core mass fraction in the SP. The horizontal dotted lines show the 1%, 5%, and 10% levels. When we estimate the total mass above $N_{\rm gas,th} = 2 \times 10^{21}$ cm$^{-2}$, the core mass fraction is ~1% for both the SP and NC. As we increase the column density threshold to only consider the denser gas, the core mass fraction increases until it reaches a maximum of 10% at $N_{\rm gas,th} = 4 \times 10^{22}$ cm$^{-2}$ for the SP and 16% at $N_{\rm gas,th} = 10^{23}$ cm$^{-2}$ for the NC.

### 4.3. Internal Dynamics of the Cores

Given the difference in mass values between the cores in the NC and the SP, we have performed a study of the internal dynamics of the identified cores. This analysis will allow us to assess the stability of the cores and look for differences between the two regions. Among the sample molecular lines, the $H^{13}CO^+$ line was used to obtain the velocity dispersion for each core. As is shown in Figures 6 and 8, this line does not show self-absorption features, and its line width is less affected by diffuse emission not related to the core. The velocity dispersion is calculated by fitting a Gaussian function to the spectral profiles derived for each core. Figure 11 shows the resulting velocity dispersion versus size relation for the cores in the NC and the SP. The cores in both regions have similar sizes, but the NC shows slightly higher velocity dispersions. Thus, this analysis suggests that the cores in the NC have a higher level of turbulence compared to the similar size cores in the SP.

Figure 11 also shows the virial parameter $\alpha_{\rm vir}$ for each core. This value is calculated using the standard equation (ignoring magnetic fields and external pressures, and assuming a uniform density profile),

$$\alpha_{\rm vir} = \frac{5\ \Delta v^2\ R_{\rm c}}{G\ M_{\rm cl}}, \quad (2)$$

where $\Delta v$ is the velocity dispersion, $R_{\rm c}$ is the radius of the clump, and $M_{\rm cl}$ is the mass. In this analysis, $M_{\rm cl}$ is obtained from the dust mass derived in 4.1. The virial parameter values are similar for the resolved cores in both regions. This is because although cores in the NC have larger velocity dispersion than in the SP, they are also more massive, resulting in similar values of $\alpha_{\rm vir}$ in both regions. In addition, all resolved cores show $\alpha_{\rm vir} < 1$, suggesting that these cores might be collapsing.

### 4.4. Gas Fragmentation

Considering the prominent differences in the core properties observed between the SP and the NC, we have performed a Jeans analysis of the gas in the regions with detected cores. If the gas in the Carina region experimented thermal fragmentation, then the Jeans mass ($M_{\rm J}$) and Jeans length ($r_{\rm J}$) represent useful parameters to compare to the properties of the cores identified in the NC and the SP. If the masses of the cores are similar to or smaller than $M_{\rm J}$ and the distances between nearby cores are similar to or smaller than $r_{\rm J}$, then thermal fragmentation explains the observed structures in a given region of a molecular cloud. This has been suggested as the predominant fragmentation process in several studies in different molecular clouds (Palau et al. 2013, 2014, 2015; Beuther et al. 2018; Sanhueza et al. 2019). Other studies, on the other side, have found core masses significantly larger than $M_{\rm J}$, suggesting that turbulent Jeans fragmentation plays a more relevant role in the generation of substructures inside clouds (Pillai et al. 2011; Wang et al. 2014).

We have estimated Jeans mass for both the NC and SP. For these calculations, the gas temperatures are the same as those used in Section 4.1. The volume densities, $n_{\rm H2}$, are estimated from the dust maps from the ATLASGAL survey, assuming a $\kappa_{0.87\ \rm mm} = 0.42$ g$^{-1}$ cm$^2$, which is an extrapolation of $\kappa_{1.3\ \rm mm} = 1$ g$^{-1}$ cm$^2$ assuming $\beta = 2$. A gas-to-dust ratio of 100 is used. We have estimated the total mass enclosed in an aperture of 20″ radius, which roughly corresponds to the clump's size as shown by the ATLASGAL maps. Thus, the volume density is estimated assuming a spherical shape of 20″ radius. For the NC, the local $n_{\rm H2} = 1.5 \times 10^5$ cm$^{-3}$, while for the SP $n_{\rm H2} = 0.7 \times 10^5$ cm$^{-3}$. With these values, we estimated $M_{\rm J} \sim 4.5\ M_\odot$ for both regions. These values are consistent with the core's masses found in the SP but are a factor of 4–5 smaller than the values of the cores in the NC.

We note that the $M_{\rm J}$ values suffer from several uncertainties given the multiple assumptions involved in the calculations. For instance, the average local gas temperatures and volume densities are estimated from current ISM conditions, which might have been significantly different at the time when the fragmentation process started. In order to investigate the variation of the $M_{\rm J}$ for several ISM conditions, Figure 12 shows a grid of Jeans mass values for a given range of $n_{\rm H2}$ and temperatures.

For the SP region, a wide range of temperatures and densities produce $M_{\rm J}$ values consistent with the estimated core mass values. For $10^4$ cm$^{-3} < n_{\rm H2} < 10^5$ cm$^{-3}$, gas temperatures going from 10 to 20 K produce $M_{\rm J}$ values that are consistent with the measured core mass values. For $n_{\rm H2} > 10^5$ cm$^{-3}$, gas temperatures have to be higher than 20 K in order to have $M_{\rm J}$ similar to the core masses detected in the SP.

On the other hand, for the NC to have a density similar to the estimated value (~$10^5$ cm$^{-3}$), the gas temperature has to be larger than 60 K for the cores' masses to be consistent with thermal fragmentation. For densities higher than $10^5$ cm$^{-3}$, the gas temperature has to be larger than 70 K to produce $M_{\rm J}$ similar to the masses of the cores identified in the NC.

The Jeans analysis presented above provides evidence for thermal fragmentation in the SP. For the NC, turbulent Jeans

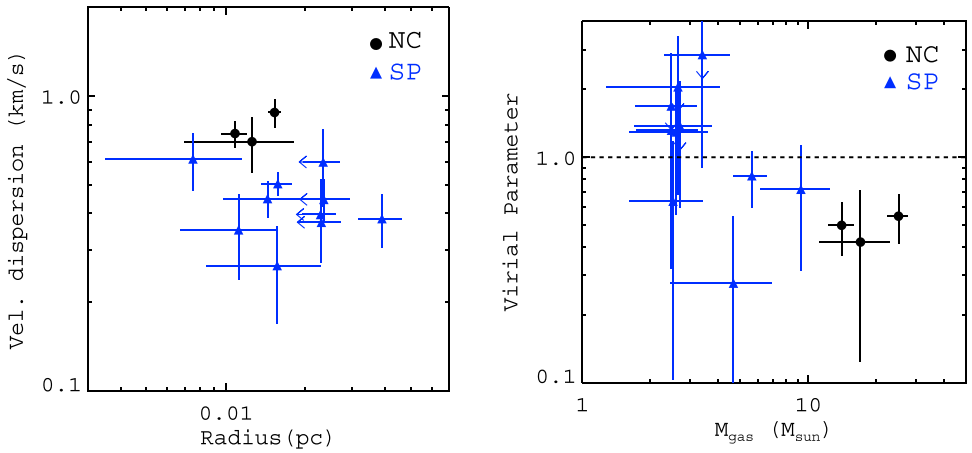


**Figure 11.** Left: size vs. velocity dispersion relation for the cores identified in the continuum map. Velocity dispersion is calculated from the spectral profile derived from the $H^{13}CO^+$ line. Filled black circles show the cores in the NC, while the blue triangles show the cores in the SP. The leftward-pointing arrows show the unresolved cores, so the sizes are upper limits. The cores in the NC have similar sizes compared to the cores at SP but show slightly higher velocity dispersions. Right: virial parameter vs. gas mass relation for the cores. Again, the downward-pointing arrows show the unresolved cores. In general, the resolved cores show virial parameters below unity, giving some evidence of collapsing structures.

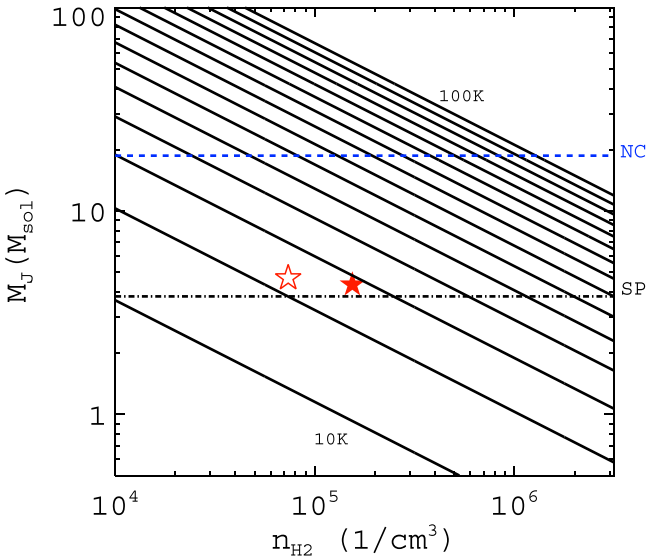


**Figure 12.** Relation between the Jeans mass ($M_J$) and the number volume density ($n_{H2}$). Each diagonal line shows a relation for a different gas temperature, from 10 K (bottom) to 100 K (up) in steps of 10 K. Horizontal dashed lines show the average core mass for the NC (blue dashed) and the SP (black dotted–dashed). The red open star shows the $M_J$ derived for average values of the volume density and temperature for the SP, while the red filled star shows the value for the NC.

fragmentation could have also played a role in the formation of high-mass cores as suggested in previous studies (Pillai et al. 2011; Wang et al. 2014). Turbulent fragmentation analysis requires a deeper knowledge of the turbulence status of the gas and cores. Therefore, the dynamics of the gas is discussed in the next section.

### 4.5. Turbulence in the Gas

Given the clear differences in stellar feedback observed in the SP and the NC, it would be helpful to have a complete picture of the velocity properties of the gas at different scales in both regions and search for similarities and differences. In order to study the internal kinematic structure of the gas in both regions, two methods are used: dendrograms and principal component analysis (PCA).

#### 4.5.1. Dendrograms

Dendrograms decompose the emission map in several structures following a tree-like configuration. In this study we made use of SCIMES, a Python package to find relevant structures into dendrograms of molecular gas emission using the spectral clustering approach described in Colombo et al. (2015). SCIMES makes use of ASTROPY,[11] a community-developed core Python package for Astronomy Astropy Collaboration et al. (2013, 2018). In the dendrograms algorithm, the largest structures are referred to as *trunks*, which are defined as being without parent structures. The *branches* are structures that are split into multiple substructures, and the *leaves* are the structures that cannot be divided into substructures. These structures are defined based on three parameters: MINVALUE, MINDELTA, and MINPIX. The MINVALUE sets the noise threshold below which no structures are identified. The MINDELTA controls the minimum intensity value required for two local maxima to be identified as separated structures. The MINPIX specifies the minimum number of pixels required to be identified as an independent structure. We have performed our analysis in the $HCO^+$ cube owing to the high brightness and broad distribution of its emission.

The decomposition was performed using MINVALUE $= 5\sigma$, MINDELTA $= 2\sigma$, and MINPIX equal to the number of pixels inside an area of three synthesized beams. We identified 584 leaves in the NC and 136 in the SP. Figure 13 shows the distributions of the velocity dispersion ($\Delta v$) of the leaves in the SP and the NC. Both distributions are roughly similar for $\Delta v < 0.3$ km s$^{-1}$. However, for $\Delta v > 0.3$ km s$^{-1}$ we observe a clear difference between the two distributions. In proportion, in the NC we detect more leaves with $\Delta v > 0.3$ km s$^{-1}$ than in the SP. The mean velocity dispersion is 0.37 km s$^{-1}$ for the NC, while for the SP it is 0.31 km s$^{-1}$. A Kolmogorov–Smirnov (K-S) test has been applied to assess whether velocity dispersion values in SP and NC are drawn from the same distribution. The K-S statistic (or D value) is equal to 0.2 and a significance level of $1.2 \times 10^{-3}$. Thus, both distributions are statistically different. In addition, a Student's *T*-statistic was

[11] http://www.astropy.org

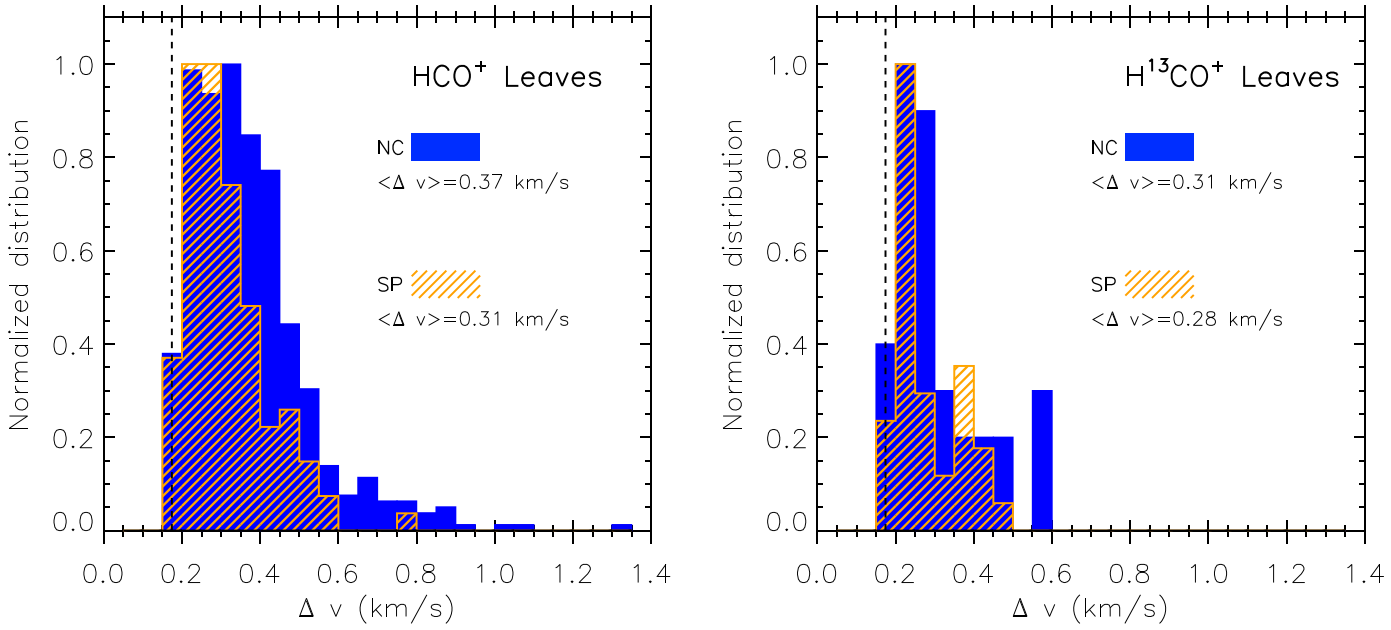


**Figure 13.** Normalized distributions of the velocity dispersion of the leaves identified by dendrograms in $HCO^+$ (left) and $H^{13}CO^+$ (right). A total of 584 leaves were identified in the NC and 184 in the SP. The filled blue histogram shows the leaves in the NC, while the hashed orange histogram shows the leaves in the SP. The vertical dashed black line shows the channel width. The distribution of the velocity dispersion of the leaves identified in the NC has a larger mean and is broader than the distribution obtained from the leaves in the SP. Thus, at the scale probed by the size of the leaves, the level of turbulence is larger in the NC than in the SP. However, the denser gas traced by $H^{13}CO^+$ shows no difference in the velocity dispersion between the two regions.

performed to assess whether the distributions of $\Delta v$ for the SP and NC have significantly different means. For the $HCO^+$ line, the *T*-test statistic is 3.8, and the *T*-test significance level is $1.8 \times 10^{-4}$. Thus, statistically, both distributions of $\Delta v$ have different means.

The difference in the velocity dispersion distribution between the two regions detected in the $HCO^+$ line is not surprising considering the level of stellar feedback that the NC is receiving from the nearby massive-star clusters Trumpler 14 and Trumpler 16. Because the $HCO^+$ line traces a wide range of gas densities, it is sensitive to the turbulent motions present in low/medium-density material that probes the pre-fragmentation gas densities. Figure 13 also shows the $\Delta v$ distribution of the leaves identified in the $H^{13}CO^+$ line cubes in both regions. This line provides information about the level of turbulence in the denser gas component in the NC and SP. We do not detect significant differences between the two regions as with $HCO^+$. The mean velocity dispersion is 0.31 and 0.28 km s$^{-1}$ for the NC and SP, respectively. A K-S test produces a *D* value equal to 0.22 and a significance level of 0.3. Thus, we cannot reject the null hypothesis in this case. Complementarily, a *T*-test study produces a statistic equal to 1.4 and a significance level equal to 0.16, confirming that both distributions are statistically similar. Thus, the difference in the level of turbulence in both regions is only detected by the low-density gas component traced by the $HCO^+$ line.

#### 4.5.2. Principal Component Analysis

In addition to the dendrogram analysis presented above, to assess the correlation between the velocity changes at different scales, we apply a PCA to the $HCO^+$ data cubes. The use of the PCA technique in the analysis of spectral-line data cubes was originally proposed by Heyer & Peter Schloerb (1997) and further developed by Brunt & Heyer (2002). In this study, we use the algorithm implemented in the TURBUSTAT Python package described in Koch et al. (2017, 2019). The PCA technique is a reduction procedure that identifies correlated components in the covariance matrix of spectral channels in a data set cube. If we write the data cube as $T(x_i, y_i, v_j) = T_{ij}$, then the covariance matrix $S_{jk}$ is given by

$$S_{jk} = \frac{1}{n}\sum_{i=1}^{n} T_{ij}T_{ik}, \quad (3)$$

where $n = n_x \times n_y$, with $n_x$ and $n_y$ giving the number of pixels in the coordinate $x$ and $y$ of the data cube, respectively. This method reconstructs the turbulent structure function, i.e., extraction of characteristic scales, by using the eigenvectors to construct a set of eigenimages (spatial structure) and eigenspectra (spectral structure). A size–line width power relation ($\Delta v \propto L^{\alpha}$) for the data is created by combining these scales over the number of eigenvalues, where the index $\alpha$ describes the turbulence regime of the data. The index $\alpha$ is different from the index $\eta$ in the energy spectrum $E(k) \propto |k|^{-\eta}$. The energy spectrum $E(k)$ describes the degree of the coherence of the velocity field over a range of spatial scales. An empirical relation between $\alpha$ and $\eta$ indexes was proposed by Brunt & Heyer (2002). From a series of models with different values of $\eta$, they found $\alpha = 0.33\eta - 0.05$ for values of $\eta$ between 1 and 3. This relation provides a calibration tool between the intrinsic velocity field statistic given by the energy spectrum and the observational measures given by the size–line width relation.

The relations between the velocity differences and the spatial scales obtained in the $HCO^+$ cubes from the PCA analysis for SP and NC are presented in Figure 14. At first sight, the SP seems to show a flatter correlation than the NC. In order to assess statistically a difference in the $\alpha$ parameter between the two regions, we have used the Bayesian inference method

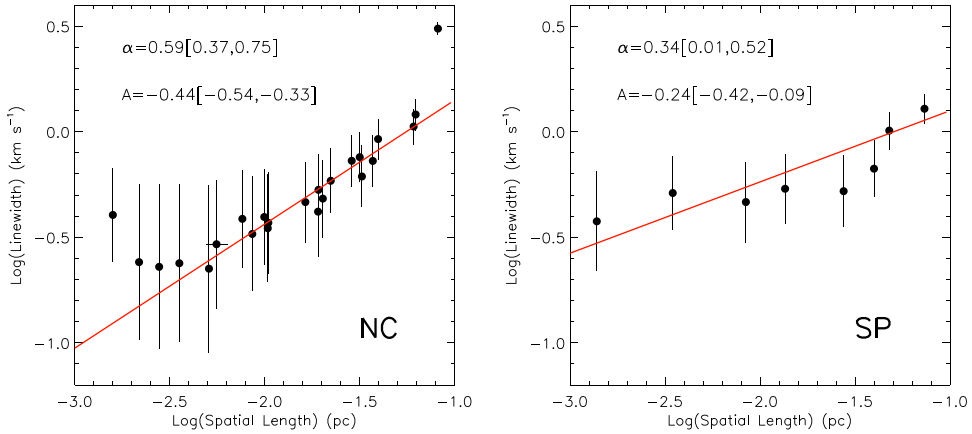


**Figure 14.** Line width vs. spatial length relationship derived from $HCO^+$ data for the NC (left) and SP (right) using the PCA technique implemented in the TURBUSTAT Python package. The red lines show the fitted power law generated by the Bayesian regression fit method for each region. The red lines are constructed by using the peak values of the parameter distributions shown in Figure 15. In the case of the NC, the outliers are removed from the fit. For each parameter, the peak value is shown, with the 90% HDI range in brackets.

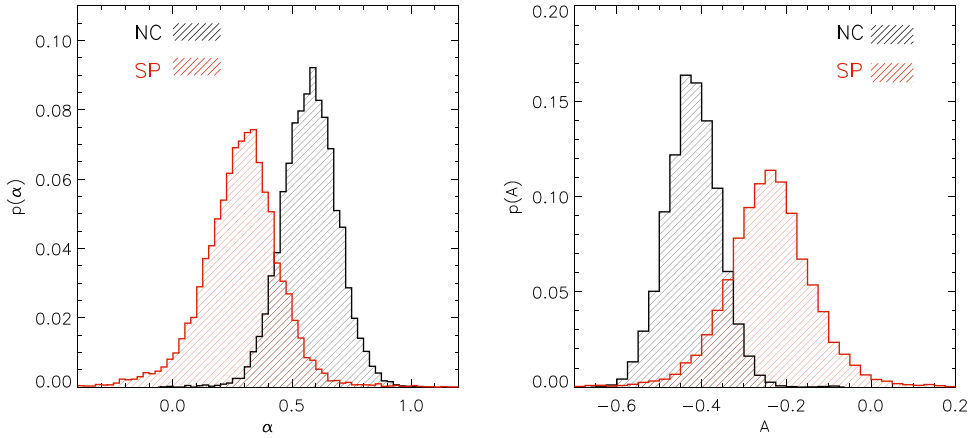


**Figure 15.** Probability distribution of the slope $\alpha$ (left) and the intercept coefficient $A$ (right) of the linear relation shown in Equation (6). The red hashed histograms show the parameter distributions obtained with SP data, and the black hashed histograms show the distributions for the NC. The $\alpha$ parameter distribution peaks at a larger value in the NC (0.59) than in the SP (0.34), but a significant overlap exists between both distributions. This implies that there is a nonnegligible probability that both relations have the same slope. If the difference exists, then it might be related to the stellar feedback activity in the NC region, which is higher than in the SP. The turbulent motion detected in the $HCO^+$ line is tracing the effect of the stellar feedback on the low-density gas in the NC region.

introduced in Kelly (2007). The Bayesian approach generates joint posterior probability distributions of the regression parameters given the observed data and draws the error in each measured quantity from some a priori defined distribution that should reflect the uncertainties in the measurements. This method has been used successfully in several previous studies of size–line width relations (Shetty et al. 2012; Rebolledo et al. 2015). According to Bayes's theorem, the posterior distribution of the parameters $\theta$ given the observed data ($x$,$y$) is given by

$$p(\theta|x,\, y) \propto p(x,\, y|\theta)p(\theta), \tag{4}$$

where $p(\theta)$ is the prior parameter distribution and $p(x,\, y|\theta)$ is the probability of the data given the parameters $\theta$. We utilized a Markov Chain Monte Carlo (MCMC) routine to sample the probability distribution of the fitting parameters through random draws. Thus, histograms of the marginal probability distributions are generated, from which we estimate the median and error for each parameter. This method provides more realistic parameter uncertainties because it accounts for the uncertainties of the dependent and independent variables of the fit at the same time. Following Kelly (2007), the fitting is performed as follows:

$$\log(y) = A + \alpha \log(x) + \epsilon_{\rm scat}, \tag{5}$$

where $\epsilon_{\rm scat}$ is the scatter about the regression line. $\epsilon_{\rm scat}$ is assumed to have a mean of 0 and dispersion $\tau$. Thus, the three parameters involved in the fitting method are $A$, $\alpha$, and $\tau$. For each scaling relation in the SP and NC, we have run $2 \times 10^4$ random draws to sample the probability distribution of the fit parameters. Because we are interested in the variations of the regression fit parameters at size scales representative of the values observed with ALMA, we have normalized the size variable by an appropriate value of 0.01pc. Thus, the linear regression is performed over the relation

$$\log\left(\frac{\text{Line width}}{\text{km s}^{-1}}\right) = A + \alpha \log\left(\frac{\text{Spatial Length}}{0.01 \text{ pc}}\right) + \epsilon_{\rm scat}. \tag{6}$$

The resulting fitted relations are shown in Figure 14. These relations are constructed by using the $\alpha$ and $A$ values corresponding to the peak of the probability distributions, which are shown in Figure 15. Along with the peak values for

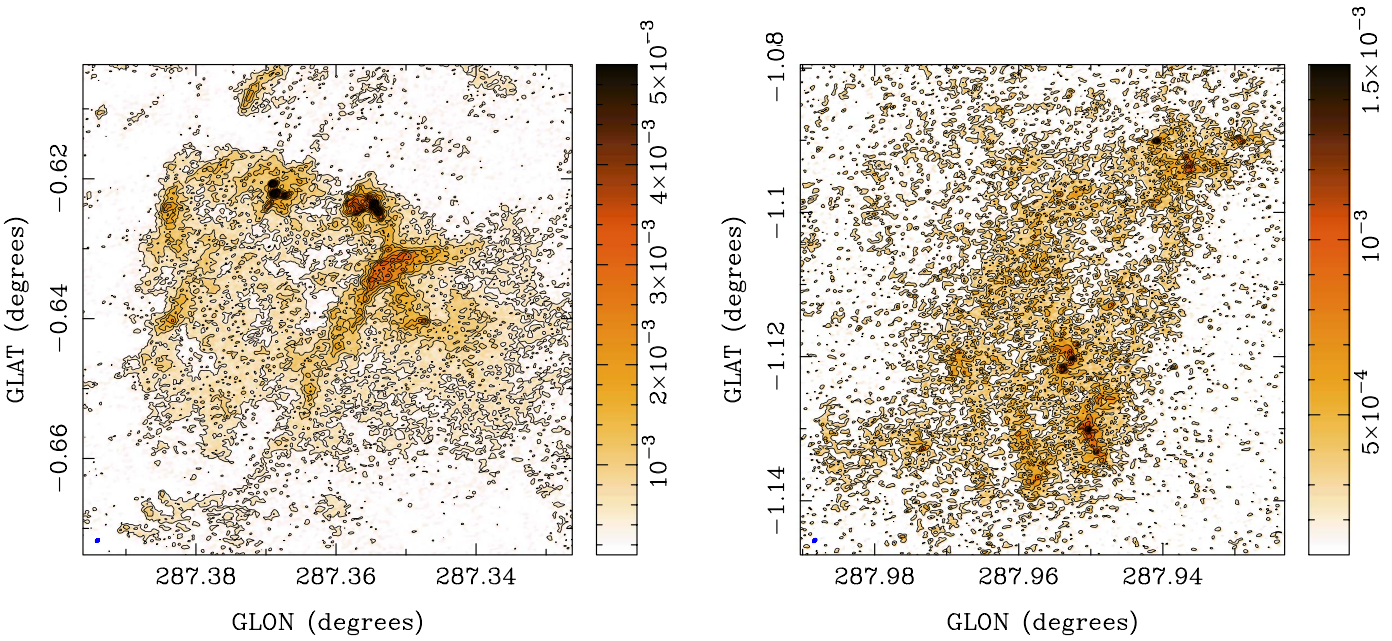


**Figure 16.** Continuum images resulting from the combination of ALMA and APEX data from the ATLASGAL survey. The left panel shows the NC, while the right panel shows the SP region. The color bar is in Jy beam$^{-1}$. The contours are given by $2 \times k \times \sigma_{\rm rms}$, where $k = 1, 2, 3, 4, 5, 6$. We clearly see a recovery of the more diffuse emission that was filtered out by ALMA interferometric observations. Our sensitivity limit defined as $2 \times \sigma_{\rm rms}$ is closed in our maps.

the parameters, we also provide the 90% high-density interval (HDI), defined as the interval that encloses 90% of the probability distribution. The HDI can be seen as a proxy for the uncertainty associated with each parameter. For the $\alpha$ parameter, the peak value is 0.59 for the NC, with a 90% HDI of [0.37, 0.75]. In contrast, the probability distribution for the $\alpha$ parameter has a peak at 0.34 for the SP, with a 90% HDI of [0.01, 0.52]. These numbers reveal that statistically there is a high probability that, given the uncertainties in the measurements of the line widths, the slope of the relation in Equation (6) is steeper in the NC than in the SP. However, given the clear overlap between the two $\alpha$ probability distributions for the NC and SP shown in Figure 15, there is a nonzero probability that both relations might have the same slope.

If we assume that the $\alpha$ parameter is in fact different between the two regions, then this difference could be interpreted as an indicator of the interaction of the stellar activity in this NC region and the surrounding medium, which is higher than in the SP. This interaction injects energy into the system at different scales in the NC, which leads to stronger correlation with the velocity fluctuations. The spatial length goes from 0.08 to 0.4 pc, which are comparable to the distance between the dense cores and the arc structures (see Section 3.1) and could be related to the fact that our observations are tracing the PDR fronts in the NC region, which might be the origin of the turbulent motion detected in the $HCO^+$ line.

### 4.6. Distribution of Column Densities

Considering the differences in the physical properties such as fragmentation and turbulence between the NC and the SP, now we direct the discussion to the internal structure of the gas distribution. One particular tool used to describe the internal structure of molecular clouds has been the volume probability density function ($\rho$-pdf). According to theories and numerical simulations, the pdf is expected to have a lognormal shape in a turbulence-dominated media where self-gravity is not important (Ostriker et al. 1999; Federrath et al. 2008). Additionally, this lognormal shape is also obtained in column density probability distributions (N-pdf) produced by simulations (Ostriker et al. 2001; Federrath et al. 2009). Observationally, detailed studies on nearby molecular clouds have revealed that while quiescent clouds show N-pdf's similar to lognormal, active star-forming clouds, in contrast, show prominent power-law wings in the high column density regime (Kainulainen et al. 2009). This difference has been interpreted as evidence for an evolutionary trend of the internal structure of molecular clouds: turbulence motions that are responsible for the lognormal shape of N-pdf's play a predominant role at very early stages of molecular cloud evolution, while power-law-like wings appear once local density enhancements, usually identified as clumps, become self-gravitating. However, other studies have proposed that the transition between lognormal and power law in an N-pdf is primarily established by the external pressure imposed by the surrounding medium on gravitationally unbound clumps (Lada et al. 2008; Kainulainen et al. 2011). Our high spatial resolution ALMA images provide an excellent laboratory to study the relation between the internal structure of clouds and physical processes such as stellar feedback and gas turbulence.

To properly sample the column density distribution, it is necessary to include all the emission associated with a particular region. Our ALMA data filtered out the large-scale emission, which is translated into missing diffuse emission in the N-pdf. To correct for the missing flux, in this study we have used APEX data from the ATLASGAL survey. As in Section 4.4, the 870 $\mu$m ATLASGAL map is extrapolated to 3 mm using $\beta = 2$ and the temperatures corresponding to each region. To do the image combination, we have used the MIRIAD task *immerge*, which is a linear method, also known as feathering, that combines in the Fourier plane single-dish and interferometric images. Figure 16 shows the resulting

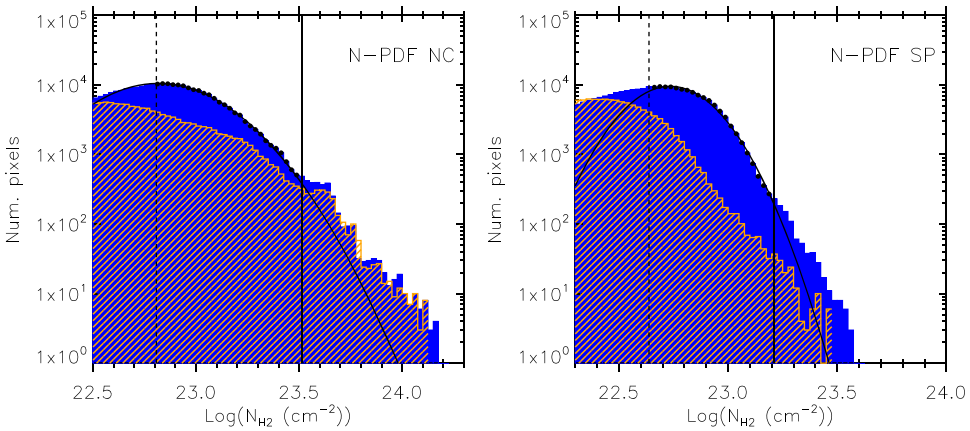


**Figure 17.** Probability distribution of the gas column density (N-pdf) in the NC (left) and the SP (right). The filled blue histogram shows the N-pdf obtained from the ALMA+APEX combined image, while the hashed orange histogram shows the N-pdf from the ALMA-only data. The black dashed line shows the $2\sigma_{\rm rms}$ sensitivity limit of the continuum maps, and the vertical black solid line illustrates the values of $N_{\rm H2,log}$ that mark the transition from Gaussian to a power-law regime. The black curved line shows the Gaussian fit to the data, considering only the bins above the sensitivity limit and below the transition column density, which are shown with black circles.

combined images of the continuum. By comparing these images with the ALMA continuum maps shown in Figures 2 and 4, it is clear to notice that the diffuse emission filtered out by our ALMA observations has been successfully recovered.

Figure 17 shows the N-pdf's derived from the combined dust continuum images for both the NC and the SP. For comparison the N-pdf's from the ALMA-only dust continuum images are also included. A transition column density ($N_{\rm H2,log}$) from lognormal to the power-law regime is evident in both regions. In the NC the $N_{\rm H2,log}$ is $\sim 3.2 \times 10^{23}$ cm$^{-2}$, while in the SP the $N_{\rm H2,log}$ is $\sim 1.7 \times 10^{23}$ cm$^{-2}$, a factor of 2 smaller. Thus, in the NC the density enhancements become self-gravitating structures at higher column densities compared to the SP. This conclusion still holds if we assume that any uncertainty in the parameters used for the calculation of the column density (dust temperature, gas-to-dust ratio, and $\beta$) affects both regions in the same way. For example, if the dust temperatures in the SP and NC are colder (or hotter) than the values we used, then the difference in the $N_{\rm H2,log}$ between the two regions still remains. The same effect is obtained if we change the gas-to-dust ratio or $\beta$ in both regions. Only when these parameters change in opposite directions can the difference in $N_{\rm H2,log}$ be larger or smaller.

Following the same approach detailed in Rebolledo et al. (2016), we have fitted a lognormal function to the N-pdf's using

$$\mathrm{Num(pixels)} = \mathrm{Num_{peak}} \times \exp\left(-\frac{(\ln(X) - \ln(X_{\rm peak}))^2}{2 \times \delta_{\rm H2}^2}\right), \quad (7)$$

where $X = N_{\rm H2}$ and $X_{\rm peak} = N_{\rm H2,peak}$. The fit was conducted only using the bins in the range $N_{\rm H2,sen} < N_{\rm H2} < N_{\rm H2,log}$, where $N_{\rm H2,sen}$ is the column density sensitivity limit. The fitted parameters are shown in Table 4.

The statistical properties of the gas volume (and column) density can be connected to the physical properties of the gas such as the Mach number and the mean magnetic field strength (Padoan et al. 1997; Ostriker et al. 2001; Goodman et al. 2009). For instance, a relation between the standard deviation of the distribution of $\ln(N_{\rm H2})$, $\sigma_{\rm lnN}$, and the sonic Mach number $\mathcal{M}$ was suggested by Padoan et al. (1997), given by

**Table 4**
Fitted Parameters of Lognormal Function to N-pdf's

| Region | $\mathrm{Num_{peak}}$ | $\log(N_{\rm H2,peak})$ | $\delta_{\rm H2}$ |
|---|---|---|---|
| NC | 10495 | 22.8 | 0.62 |
| SP | 9554 | 22.7 | 0.39 |

$\sigma^2_{\rm lnN} = \ln(1 + \mathcal{M}^2\gamma^2)$, where $\gamma \sim 0.5$. For a true lognormal distribution, $\sigma_{\rm lnN}$ is equal to the $1\sigma$ standard deviation of a Gaussian fit given by $\delta_{\rm H2}$.

Under the model proposed by Padoan et al. (1997), wider N-pdf's are observed in regions with a high level of turbulence as traced by $\mathcal{M}$. This is consistent with the N-pdf's differences observed between the NC and the SP. Both analyses presented in Sections 4.5.1 and 4.5.2 revealed stronger turbulence in the NC compared to the SP. Table 4 shows a value of $\delta_{\rm H2} = 0.62$ for the NC. In contrast, for the SP $\delta_{\rm H2} = 0.39$. This implies a $\mathcal{M} = 1.37$ for the NC and $\mathcal{M} = 0.81$ for the SP, which indicates that the level of turbulence in NC is supersonic while in the SP it is subsonic. The analysis presented here ignores the contribution from magnetic field in the relation between the statistical properties of the gas density distribution and the physical properties of the gas. If a magnetic field is present, then the relation given by Padoan et al. (1997) changes and depends on the magnetosonic Mach number $\mathcal{M}_{\rm F}$.

Figures 2 and 4 showed that the diffuse dust emission at 3 mm is weak, especially in the SP. Thus, our N-pdf's are probably affected by our sensitivity limit, more strongly at the low column density side of the distribution. Additionally, we extrapolated the 0.87 mm ATLASGAL map to 3 mm to produce an ALMA+APEX combined image that recovers the total flux. This extrapolation strongly depends on the parameters used such as $\beta$ and dust temperature, increasing the uncertainty in the flux distribution of the combined ALMA +APEX continuum map.

Another caveat of the analysis presented in this section is the contamination of free–free emission in the continuum map at 3 mm. As was explained in Section 3.1.1, the identification of cores in the NC was limited to the brightest sources to avoid false identification of low-mass cores in emission associated with free–free. In this section, on the contrary, it is assumed that all the emission in the continuum is from dust. Thus, our

N-pdf's are probably affected by the emission of ionized gas. However, the combined continuum images shown in Figure 16 are very similar to the integrated intensity maps from the HCN and $HCO^+$ lines shown in Figure 2, providing some evidence that the continuum maps are dominated by the dust emission.

In a recent paper, Alves et al. (2017) studied the effect of the boundary of a surveyed area of a given molecular cloud on the shape of the observed column density distribution. In their study, they considered molecular clouds in different evolutionary stages from diffuse to star-forming ones. They found that if the column density value at the last closed contour is used as the completeness limit of the column density pdf, then the shape of the N-pdf is always a power law and no evidence for a lognormal distribution is observed. They concluded that the lognormal shape observed in previous works might be related to incompleteness in the sampling of the column density distribution if pixels belonging to open contours are included. From Figure 16 it is clear to notice that our limiting column density, chosen to be $2\sigma_{\rm rms}$, corresponds to a closed contour in our dust maps in both regions. However, although the peaks of the lognormal distributions shown in Figure 17 are above this sensitivity limit, the values are fairly close. Thus, our conclusions about the shape of the N-pdf's have to be reviewed once brighter continuum maps become available in the future.

## 5. Summary

We have performed high spatial observations toward two regions in one of the more extreme massive star-forming clouds in the Galaxy, the Carina Nebula Complex. One region is located in the heart of the nebula and heavily affected by the feedback coming from the massive stellar clusters present in the region. The other region is located farther south, much more distant from the massive stellar clusters and less affected by their feedback. With an angular resolution of $\sim 3''$, our Band 3 ALMA observations have allowed us to obtain a detailed view of the internal structure of two regions with significantly different physical conditions. The main results of our study are summarized as follows:

1. The continuum maps revealed several structures inside both regions. In the region located in the NC, the diffuse emission shows two arc-like structures that we relate to ionization fronts produced by the radiation field coming from the massive-star clusters Trumpler 14 and Trumpler 16. On the other hand, continuum emission is weak in the SP, and our ALMA data are not sensitive enough to detect it.
2. In the NC we detected three cores, while in the SP only 10 cores have been identified. The sizes of the cores are roughly similar, with a mean radius of $\sim$0.017 pc (3400 au). However, the cores in the NC are more massive than the cores in the SP, with a mean mass of 19.4 $M_\odot$ in the NC versus 3.8 $M_\odot$ in the SP, i.e., a factor of $\sim$5 difference. This represents one of the most remarkable differences between these two regions, suggesting that the fragmentation process proceeded differently in the NC, where the stellar feedback is stronger compared to the SP.
3. The HCN and $HCO^+$ lines, which are the brightest among the observed sample, show a complex gas distribution in both regions. Both lines trace a wide column density range, from diffuse to dense gas. In the NC, the arcs identified in continuum map structures are better delineated by the line emission from these molecules, revealing the presence of PDRs produced by the nearby massive stars. Multiple velocity components are detected in the NC over a 30 km $s^{-1}$ range. In the SP the emission from these lines is 4–5 times weaker and extends over 20 km $s^{-1}$.
4. Both compact and diffuse SiO emission is clearly detected in the NC. The compact emission is spatially coincident with the cores detected in the continuum, suggesting the presence of outflows. On the other hand, the diffuse SiO emission directly follows the arc-like structures detected in the continuum and in the brighter molecular line maps. We interpret this as evidence of the presence of photodissociated gas produced by the energy feedback of the nearby massive stars. In strong contrast, in the SP we only detect compact SiO in a couple of positions near a single core.
5. The Jeans mass is $\sim$4.5 $M_\odot$ in the NC and the SP regions, which is similar to the core masses detected in the SP, and a factor of 4 smaller than the mean core mass in the NC. We conclude that the observed core masses in the SP are consistent with thermal fragmentation, but in the NC, turbulent Jeans fragmentation might explain the high masses of the identified cores. Two different analysis techniques, dendrograms and PCA, provided evidence for a higher level of turbulence of the gas in the NC compared to the SP region.
6. The gas column density probability functions, or N-pdf's, derived from the continuum maps show a lognormal shape at low column densities and a power law at large column density. The transition column density is $N_{\rm H2} \sim 3.\ 2 \times 10^{23}\,{\rm cm}^{-2}$ in the NC and $N_{\rm H2} \sim 1.\ 7 \times 10^{23}\,{\rm cm}^{-2}$ in the SP. If this transition marks the column density at which the structures become self-gravitating, then this process happens at higher column densities in the NC compared to the SP.
7. A lognormal function fit to the N-pdf's revealed a wider distribution of the column density in the NC compared to the SP. If a relationship between the width of the lognormal distribution and the Mach number $\mathcal{M}$ exists, as has been proposed in simulations, then $\mathcal{M}$ is larger in the NC, providing further evidence for a higher level of turbulence in this region owing to its exposure to the massive stellar feedback.

This paper makes use of the following ALMA data: ADS/JAO.ALMA#2016.1.01609.S. ALMA is a partnership of ESO (representing its member states), NSF (USA) and NINS (Japan), together with NRC (Canada), *MOST* and ASIAA (Taiwan), and KASI (Republic of Korea), in cooperation with the Republic of Chile. The Joint ALMA Observatory is operated by ESO, AUI/NRAO, and NAOJ. The National Radio Astronomy Observatory is a facility of the National Science Foundation operated under cooperative agreement by Associated Universities, Inc. D.R. acknowledges support from the ARC Discovery Project grant DP130100338 and from CONICYT through project PFB-06 and project Fondecyt 3170568. G.G. acknowledges support from CONICYT project Basal AFB-170002. S.-N. X.M. is a member of the International Max-Planck Research School at the Universities of Bonn and Cologne (IMPRS). P.S. was financially supported by

Grant-in-Aid for Scientific Research (KAKENHI No. 18H01259) of the Japan Society for the Promotion of Science (JSPS).

## ORCID iDs

David Rebolledo https://orcid.org/0000-0002-1010-583X
Andrés E. Guzmán https://orcid.org/0000-0003-0990-8990
Yanett Contreras https://orcid.org/0000-0002-6388-3635
Patricio Sanhueza https://orcid.org/0000-0002-7125-7685
Viviana Guzmán https://orcid.org/0000-0003-4784-3040

## References

Alves, J., Lombardi, M., & Lada, C. J. 2017, A&A, 606, L2
Astropy Collaboration, Robitaille, T. P., Tollerud, E. J., et al. 2013, A&A, 558, A33
Astropy Collaboration, Price-Whelan, A. M., Sipőcz, B. M., et al. 2018, AJ, 156, 123
Avison, A., Quinn, L. J., Fuller, G. A., et al. 2016, MNRAS, 461, 136
Beuther, H., Mottram, J. C., Ahmadi, A., et al. 2018, A&A, 617, A100
Brooks, K. J., Cox, P., Schneider, N., et al. 2003, A&A, 412, 751
Brooks, K. J., Storey, J. W. V., & Whiteoak, J. B. 2001, MNRAS, 327, 46
Brunt, C. M., & Heyer, M. H. 2002, ApJ, 566, 276
Colombo, D., Rosolowsky, E., Ginsburg, A., Duarte-Cabral, A., & Hughes, A. 2015, MNRAS, 454, 2067
Contreras, Y., Rebolledo, D., Breen, S. L., Green, A. J., & Burton, M. G. 2019, MNRAS, 483, 1437
Federrath, C., Klessen, R. S., & Schmidt, W. 2008, ApJL, 688, L79
Federrath, C., Klessen, R. S., & Schmidt, W. 2009, ApJ, 692, 364
Federrath, C., Rathborne, J. M., Longmore, S. N., et al. 2016, ApJ, 832, 143
Gardner, F. F., & Morimoto, M. 1968, AuJPh, 21, 881
Gerin, M., Goicoechea, J. R., Pety, J., & Hily-Blant, P. 2009, A&A, 494, 977
Goldsmith, P. F., & Kauffmann, J. 2017, ApJ, 841, 25
Goodman, A. A., Pineda, J. E., & Schnee, S. L. 2009, ApJ, 692, 91
Green, J. A., Caswell, J. L., Fuller, G. A., et al. 2009, MNRAS, 392, 783
Green, J. A., Caswell, J. L., Fuller, G. A., et al. 2012, MNRAS, 420, 3108
Guilloteau, S., & Baudry, A. 1981, A&A, 97, 213
Heiderman, A., Evans, N. J., II, Allen, L. E., Huard, T., & Heyer, M. 2010, ApJ, 723, 1019
Heyer, M. H., & Peter Schloerb, F. 1997, ApJ, 475, 173
Kainulainen, J., Beuther, H., Banerjee, R., Federrath, C., & Henning, T. 2011, A&A, 530, A64
Kainulainen, J., Beuther, H., Henning, T., & Plume, R. 2009, A&A, 508, L35
Kauffmann, J., Goldsmith, P. F., Melnick, G., et al. 2017, A&A, 605, L5
Keene, J., Schilke, P., Kooi, J., et al. 1998, ApJL, 494, L107
Kelly, B. C. 2007, ApJ, 665, 1489
Koch, E. W., Rosolowsky, E. W., Boyden, R. D., et al. 2019, AJ, 158, 1
Koch, E. W., Ward, C. G., Offner, S., Loeppky, J. L., & Rosolowsky, E. W. 2017, MNRAS, 471, 1506
Lada, C. J., Muench, A. A., Rathborne, J., Alves, J. F., & Lombardi, M. 2008, ApJ, 672, 410
Loughnane, R. M., Redman, M. P., Thompson, M. A., et al. 2012, MNRAS, 420, 1367
McKee, C. F., & Ostriker, E. C. 2007, ARA&A, 45, 565
Mullins, A. M., Loughnane, R. M., Redman, M. P., et al. 2016, MNRAS, 459, 2882
Ostriker, E. C., Gammie, C. F., & Stone, J. M. 1999, ApJ, 513, 259
Ostriker, E. C., Stone, J. M., & Gammie, C. F. 2001, ApJ, 546, 980
Padoan, P., Nordlund, A., & Jones, B. J. T. 1997, MNRAS, 288, 145
Palau, A., Ballesteros-Paredes, J., Vázquez-Semadeni, E., et al. 2015, MNRAS, 453, 3785
Palau, A., Estalella, R., Girart, J. M., et al. 2014, ApJ, 785, 42
Palau, A., Fuente, A., Girart, J. M., et al. 2013, ApJ, 762, 120
Pillai, T., Kauffmann, J., Wyrowski, F., et al. 2011, A&A, 530, A118
Rathborne, J. M., Longmore, S. N., Jackson, J. M., et al. 2015, ApJ, 802, 125
Rebolledo, D., Burton, M., Green, A., et al. 2016, MNRAS, 456, 2406
Rebolledo, D., Green, A. J., Burton, M., et al. 2017, MNRAS, 472, 1685
Rebolledo, D., Wong, T., Xue, R., et al. 2015, ApJ, 808, 99
Roccatagliata, V., Preibisch, T., Ratzka, T., & Gaczkowski, B. 2013, A&A, 554, A6
Rodríguez-Fernández, N. J., Tafalla, M., Gueth, F., & Bachiller, R. 2010, A&A, 516, A98
Rosolowsky, E., & Leroy, A. 2006, PASP, 118, 590
Sanhueza, P., Contreras, Y., Wu, B., et al. 2019, ApJ, 886, 102
Sanhueza, P., Jackson, J. M., Foster, J. B., et al. 2012, ApJ, 756, 60
Schenewerk, M. S., Snyder, L. E., Hollis, J. M., Jewell, P. R., & Ziurys, L. M. 1988, ApJ, 328, 785
Schilke, P., Pineau des Forêts, G., Walmsley, C. M., & Martín-Pintado, J. 2001, A&A, 372, 291
Schuller, F., Menten, K. M., Contreras, Y., et al. 2009, A&A, 504, 415
Seo, Y. M., Goldsmith, P. F., Walker, C. K., et al. 2019, ApJ, 878, 120
Shetty, R., Beaumont, C. N., Burton, M. G., Kelly, B. C., & Klessen, R. S. 2012, MNRAS, 425, 720
Smith, N. 2006, MNRAS, 367, 763
Smith, N., Bally, J., & Walborn, N. R. 2010a, MNRAS, 405, 1153
Smith, N., & Brooks, K. J. 2008, in Handbook of Star Forming Regions, Volume II, ed. B. Reipurth (San Francisco, CA: ASP), 138
Smith, N., Povich, M. S., Whitney, B. A., et al. 2010b, MNRAS, 406, 952
Solomon, P. M., Rivolo, A. R., Barrett, J., & Yahil, A. 1987, ApJ, 319, 730
Stephens, I. W., Jackson, J. M., Whitaker, J. S., et al. 2016, ApJ, 824, 29
Wang, K., Zhang, Q., Testi, L., et al. 2014, MNRAS, 439, 3275
Zinchenko, I., Henkel, C., & Mao, R. Q. 2000, A&A, 361, 1079